Disruption of the grid cell network in a mouse model of early Alzheimer's disease

Authors: Johnson Ying[1,2], Alexandra T. Keinath[1], Raphael Lavoie[1], Erika Vigneault[1], Salah El Mestikawy[1,2], Mark P. Brandon[1,2,*]

Affiliations:

[1]Department of Psychiatry, Douglas Hospital Research Centre, McGill University, Montreal, QC, Canada.

[2]Integrated Program in Neuroscience, McGill University, Montreal, QC, Canada.

*Correspondence to: mark.brandon@mcgill.ca

Abstract

Early-onset familial Alzheimer's disease (AD) is marked by an aggressive buildup of amyloid beta (Aβ) proteins, yet the neural circuit operations impacted during the initial stages of Aβ pathogenesis remain elusive. Here, we report a coding impairment of the medial entorhinal cortex (MEC) grid cell network in a transgenic mouse model of familial AD that over-expresses Aβ throughout the hippocampus and entorhinal cortex. Grid cells showed reduced spatial periodicity, spatial stability, and synchrony with interneurons and head-direction cells. In contrast, the spatial coding of non-grid cells within the MEC, and place cells within the hippocampus, remained intact. Grid cell deficits emerged at the earliest incidence of Aβ fibril deposition and coincided with impaired spatial memory performance in a path integration task. These results demonstrate that widespread Aβ-mediated damage to the entorhinal-hippocampal circuit results in an early impairment of the entorhinal grid cell network.

Main Text

The molecular and synaptic underpinnings of Aβ pathology during the earliest stages of familial AD are well-documented, but the impact that these changes have on neural coding has not been resolved[1,2]. The emergence of spatial memory deficits in patients with preclinical AD and those with Mild Cognitive Impairment with high levels of cerebrospinal fluid Aβ suggest that initial Aβ pathology exerts its earliest impact on the neural systems that support spatial memory[3,4]. Extensive work in both animals and humans have pinpointed the MEC-hippocampal circuit as essential brain regions for spatial memory performance[5–7]. At the level of neural coding, the MEC-hippocampal circuit contains a myriad of spatially-tuned cell types including place cells in the hippocampus, as well as grid cells, head direction cells, and non-grid spatially-selective cells in the MEC[8–12]. Decades of theoretical work have proposed how these functional cell types work in concert to support spatial memory[13–17]. Yet, it remains unknown how these spatially-tuned populations are impacted at the earliest stages of Aβ-mediated pathogenesis when spatial memory is impaired.

To address this, we used a J20 transgenic mouse model of familial AD that expresses a mutant form of human amyloid precursor protein (APP), referred to here as 'APP mice'[18]. In this model, elevated and comparable levels of soluble Aβ throughout the entorhinal cortex and hippocampus are present at 3 months of age[19]. By 5-7 months of age, small Aβ fibrils are detectable in the hippocampus but neither of these regions demonstrate widespread amounts of Aβ plaques that are indicative of late AD pathology[19]. We confirmed that APP mice expressed little-to-no plaques by 6 months of age in the MEC and hippocampus (**Supplementary Fig. 1**). Between 3-7 months of age, APP mice exhibit several amyloid-related processes that we refer to collectively as 'early Aβ pathology'. These include neuroinflammation, 10-20%

neuronal loss, and reduced presynaptic terminal density throughout the entorhinal cortex and hippocampus (detailed pathology description in Methods, *Subjects*)[20–23].

We obtained *in vivo* recordings of MEC neurons (n cells = 4524) from 38 APP transgenic and 30 non-transgenic (nTG) littermates as they foraged for water droplets in an open field arena (*Summary of MEC recordings*, **Tables 1, 2**; *MEC Tetrode locations*, **Supplementary Fig. 2**). We observed an age-related disruption in the spatial periodicity of grid cells in APP mice (**Fig. 1a-d, Supplementary Figs. 3, 4, 5**). Young APP mice (3-4.5 months) had grid cells with tuning comparable to those of age-matched nTG mice (**Fig. 1**). In contrast, grid cells recorded in adult (4.5-7 months) APP mice exhibited reduced spatial periodicity and spatial information (bits/spike) in comparison to those from young APP mice and age-matched nTG mice (**Fig. 1**). Peak spatial firing and mean firing rates of grid cells did not reliably differ between groups and across age (**Fig. 1e**). A two-way ANOVA was conducted to determine the effects of age and genotype on grid score between groups. A significant interaction effect was discovered, supporting the view that grid cell spatial periodicity is reduced across age in APP mice (*ANOVA*, age main effect: $P = 0.0000002$; genotype main effect: $P = 0.024$; interaction effect: $P = 0.00062$, **Supplementary Fig. 6**). To ensure that these results are not biased by oversampling the same cells across days, we removed duplicate grid cells and re-ran our analyses. Grid cell spatial periodicity remained impaired in adult APP mice, and the significant interaction effect persisted (*ANOVA*, age main effect: $P = 0.00045$; genotype main effect: $P = 0.013$; interaction effect: $P = 0.046$, **Supplementary Fig. 7**).

In contrast to the age-dependent impairment observed in grid cells, entorhinal head direction cells, which encode the orientation of the animal's head in polar coordinates[10], did not differ in their directional tuning or firing rates between groups or across age (**Fig. 2a, Supplementary Fig. 8**). Similarly, there was no difference between groups in the average firing

field size of non-grid spatially-tuned neurons, which fire in a non-periodic but spatially reliable manner (**Fig. 2b, Supplementary Fig. 8**). Mean firing rates did not differ between groups, but spatial peak firing rates were, however, oddly elevated in adult nTG mice (**Fig. 2b**).

To examine if spatial coding by downstream hippocampal place cells was disrupted when adult APP mice exhibit a degraded grid cell code, we obtained *in vivo* recordings from region CA1 of the hippocampus (n cells = 992) from 6 adult APP and 6 adult nTG mice (*Summary of CA1 recordings*, **Tables 3, 4;** *CA1 Tetrode locations*, **Supplementary Fig. 9**). Place cells in adult APP and nTG mice were similarly tuned for spatial location and had similar peak spatial and mean firing rates (**Fig. 2c, Supplementary Fig. 8**). Spatial tuning remained largely preserved across groups when varying our cell selection threshold (spatial peak firing rates between 0 and 8 Hz), with the exception of thresholds less than 1 Hz (**Fig. 2d**). Mean firing rates were higher in APP place cells at peak firing selection thresholds of 6 Hz and greater, suggesting that the overall mean firing rate is higher in adult APP mice than those in adult nTG mice (**Fig. 2d**). These results demonstrate that the hippocampal place code remains grossly intact when the entorhinal grid code is degraded in adult APP mice, mirroring findings observed in early development and during inactivation of the medial septum[24–26]. Our findings are consistent with previous work showing that the spatial tuning of place cells in Tg2576 APP mice remained intact at the earliest incidence of Aβ plaques, but was subsequently impaired when Aβ plaques become widespread[27]. Moreover, our results suggest that impaired grid coding in adult APP mice is not the result of disrupted feedback from the hippocampus[28].

Prior work has reported a selective disruption of grid cell spatial periodicity without impairment of other spatial codes when the power of entorhinal theta oscillations (6-10 Hz) is reduced via inactivation of the medial septum[25,26]. We therefore examined entorhinal theta

oscillations across nTG and APP mice and found that theta power remained intact in adult APP mice across running speeds (*ANCOVA*, APP-a vs nTG-a, main effect: $P = 0.99$; interaction between running speed and theta power: $P = 0.096$; APP-a vs APP-y, main effect: $P = 0.051$; interaction between running speed and theta power: $P = 0.56$; **Fig. 2e**). In both young and adult APP mice, the overall baseline frequency of theta oscillations was lower while the gain in theta frequency across running speeds was preserved (*ANCOVA*, APP-a vs nTG-a, main effect: $P = 0.01$; interaction between running speed and frequency: $P = 0.51$; APP-y vs nTG-y, main effect: $P = 0.0001$; interaction between running speed and frequency: $P = 0.82$; **Fig. 2e**), revealing that the baseline frequency of theta oscillations was reduced in APP mice prior to the onset of grid cell disruption. Theta frequency reduction in both young and adult APP mice was roughly 0.2 Hz across all running speeds (**Supplementary Fig. 10**). Assuming that this reduction in theta frequency has no effect on grid cell periodicity in young APP mice, these results indicate that impaired grid cell coding in adult APP mice cannot be explained by a disruption of the theta-generating circuit.

Speed cells in the MEC encode the animal's running speed by firing rate and are assumed to provide a speed signal for grid cell formation[29]. To determine if impaired speed cells could explain the disrupted grid cell periodicity in adult APP mice, we examined the running speed vs firing rate correlation of MEC cells that were not characterized as either grid cells, head direction cells and non-grid spatially-tuned cells (**Supplementary Fig. 11**). No significant differences were found between groups when varying our cell selection threshold (running speed vs firing rate correlation values between 0.1 and 0.9), suggesting that MEC speed cells remained unaffected by APP pathology (**Supplementary Fig. 11a**). Running speed vs firing rate correlations of grid cells

was also non-significant between groups, providing further evidence for an intact speed code (**Supplementary Fig. 11b, c**).

To characterize the nature of reduced grid cell periodicity in adult APP mice, we examined the spatial firing properties of grid cells in further detail. In contrast to grid cells recorded in adult nTG mice, grid cells in adult APP mice exhibited larger firing fields when accounting for differences in spatial scale (**Fig. 3a**). We reasoned that an increase in field size in adult APP mice could reflect a drifting or unstable grid pattern over time. Consistent with this, a partitioned rate map stability analysis revealed that the overall grid pattern in adult APP mice exhibited reduced spatial stability (**Fig. 3b-d**). The reduced stability of grid cells in adult APP mice was not due to changes in the orientation of grid fields, indicating that instability reflected an inconsistent spatial phase of the grid pattern over time (**Fig. 3e**). In contrast, non-grid spatially-tuned cells and hippocampal place cells of adult APP mice remained spatially stable across time (**Fig. 3b-d**). A two-way ANOVA was conducted to further confirm that the spatial instability was specific to grid cells, but not non-grid spatially-tuned cells and place cells in adult APP mice. The ANOVA design's factors consisted of genotype and cell type, and both significant main and interaction effects were discovered (*ANOVA*, genotype main effect: $P = 0.0038$; genotype main effect: $P = 0.0084$; interaction effect: $P = 0.013$, **Supplementary Fig. 12**). Given the significant interaction effect, post-hoc pairwise comparisons using Tukey's Test revealed greater spatial instability in APP-a grid cells, but not in APP-a non-grid spatially-tuned cells or place cells (*Tukey's test*, APP-a grid cells vs. nTG-a grid cells: $P = 0.0064$; APP-a non-grid cells vs. nTG-a non-grid cells: $P = 1$; APP-a place cells vs. nTG-a place cells: $P = 0.99$). Instability persisted in adult APP grid cells when partition lengths were extended from 3 minutes to 5, 6 and 10 minutes (**Supplementary Fig. 13**). Consistent with previous literature[30,31], positional coverage and running speeds were higher

in adult APP mice, suggesting that greater displacements were not biased by insufficient exploration of the open field environment (**Supplementary Fig. 14**).

Given that inhibition constitutes a major input for grid cell generation[32,33], we analyzed the firing properties of interneurons in APP mice. Across age, mean firing rates became elevated in adult APP mice (*ANOVA*, genotype main effect: $P = 0.0038$; genotype main effect: $P = 0.0084$; interaction effect: $P = 0.013$, **Supplementary Figs. 15, 16**), alluding to possible changes in inhibitory networks within the MEC. In particular, we noted that a significant proportion of interneurons in young and adult APP mice had slower theta rhythmicity and theta power, suggesting a potential early impairment in spike timing dynamics between grid cells and interneurons preceding the loss of grid cell spatial periodicity (**Supplementary Fig. 15, 16**). By computing spike-timing cross-correlations between simultaneously recorded MEC cells, we observed that synchrony between grid cells and interneurons were qualitatively reduced in young APP mice in comparison to nTG mice (**Fig. 4a-b**). In fact, young APP grid cells and interneurons appeared anti-synchronous at a temporal lag of ~25ms, suggesting the start of an early impairment of the grid cells' ability to integrate inhibitory signals. Surprisingly, the same pattern was also qualitatively observed between grid cells and head direction cells, which appeared to worsen across age (**Fig. 4a-b**). However, in both cases, non-parametric statistics between groups could not directly validate any of these claims (**Fig. 4c**).

To better interpret these findings, a two-way ANOVA was conducted to determine the effects of age and genotype on the mean co-activity within a 25 ms time window for grid cell-interneuron and grid cell-head direction cell pairs (**Supplementary Fig. 17**). There was no significant interaction effect in either group (*ANOVA:* grid-interneuron interaction effect: $P = 0.091$; grid-head direction interaction effect: $P = 0.083$, **Supplementary Fig. 17**), confirming the

absence of any age-dependent reduction in synchrony. However, there was a significant main effect of genotype in both groups, indicating that grid cell-interneuron and grid cell-head direction cell synchrony were impaired overall in both young and adult APP mice (*ANOVA:* grid-interneuron genotype main effect: $P = 0.000013$; grid-head direction genotype main effect: $P = 0.012$, **Supplementary Fig. 17**). In support of this view, synchrony was significantly lower in adult APP mice compared to adult nTG mice, and was unaffected compared to young APP mice (**Fig. 4c**). However, the lack of statistical significance between young APP and young nTG mice implies that this reduction may be milder in the earliest stages of pathology (**Fig. 4c**). These findings are significant in two ways. First, given the importance of inhibitory and head direction information for grid cell spatial firing[32–34], these results suggest that disrupted grid cell spatial periodicity across age in APP mice (**Fig. 1**) arises in part due to the decoupling of grid cells from inhibitory and head direction inputs within the local MEC network. Second, this decoupling starts (albeit mildly) from an age when grid cell spatial periodicity is still intact, suggesting that grid cell coding is affected at age points preceding the complete loss of spatial periodicity.

Prior work has shown that APP mice exhibit spatial memory deficits on the Morris water maze and the radial arm maze by as early as 3-4 months of age[21,30]. Given the proposed role of grid cells in supporting path integration[17,35], we hypothesized that APP mice would also experience spatial memory deficits related to path integration. To test this hypothesis, we conducted a path integration task to assess the animals' ability to return directly to their refuge after finding a food pellet in an open field in complete darkness with an independent, non-implanted cohort of APP and nTG mice (n mice = 12 APP-y, 9 APP-a, 10 nTG-y, 8 nTG-a; **Fig. 5a, Supplementary Fig. 18a**). APP and nTG mice demonstrated a similar inclination to return to the refuge prior to consumption of the pellet (**Supplementary Fig. 18b-d**). However, we observed that APP mice

were impaired in all measures of path integration ability relative to age-matched controls, with the greatest behavioral deficits in adult APP mice. In particular, the probability of arriving at the refuge during the initial wall contact decreased in APP mice across age (APP-a: 29%, APP-y: 38%, nTG-y: 58%, nTG-a: 57%; **Fig. 5b, c**), suggesting that they had a greater difficulty in estimating their position relative to the refuge. In further support of this possibility, adult APP mice exhibited increased error in both their initial heading direction and the angular difference between the refuge and the first wall encountered during the return trajectory (**Fig. 5d, e**). With regards to overall navigational efficiency, adult APP mice travelled longer distances to return to the refuge and exhibited greater thigmotaxis by spending a larger proportion of the return path along the periphery of the environment (**Fig. 5d, e**). All groups showed improved performance when visual cues were made available (**Supplementary Fig. 19**), though APP mice remained impaired across all measures of task performance which worsened with age (**Supplementary Fig. 20**). Together, these results show that path integration abilities decline with age in APP mice, closely mirroring the time course of the spatial coding deficits observed in the grid cell network.

Lastly, we characterized which molecular changes could explain these early network alterations in the entorhinal-hippocampal circuit. A recent meta-analysis confirmed that synapse loss and changes in synaptic marker expression are major events in AD pathogenesis[36]. Likewise, altered synaptic function could also affect circuit function such as grid cell coding that is known to require both excitatory and inhibitory drive[28,32,33]. For these reasons, we carried out immunoautoradiography in the MEC and CA1 to visualize and quantify the expression of synaptic markers that include VGLUT1, VGLUT3, VAChT, VGAT and NR1 (**Supplementary Fig. 21**). VGLUT1, VGLUT3 VAChT and VGAT are neurotransmitter transporters whereas NR1 is a subunit of NMDA receptors that was previously shown to be necessary for both grid cell integrity

and path integration ability[35] (detailed marker descriptions in Methods, *Immunoautoradiographic labelling of synaptic markers*).

To interpret the most robust pathological changes, we ran linear mixed models to pinpoint which marker expression levels were most affected by early Aβ pathology. Out of the ten experimental groups, two cases were significantly modulated by the effect of the subject's genotype: VGLUT3 in the MEC and VGLUT1 in CA1 (*VGLUT3 in MEC*, genotype effect: $P < 0.01$; *VGLUT1 in CA1*, genotype effect: $P < 0.01$; **Supplementary Fig. 22**). We observed an increase of VGLUT3 in both young and aged APP mice, indicating that CCK-positive interneurons are exerting greater influence in inhibitory circuits within the MEC (**Supplementary Fig. 23a, b, Supplementary Fig. 24**). However, VGAT levels were not significantly different (**Supplementary Figs. 21, 22**), suggesting that early Aβ pathology targets a specific inhibitory circuit while sparing overall inhibitory drive. Taken together with our spike time cross-correlation analysis (**Fig. 4**), these findings pinpoint inhibitory mechanisms as one of the earliest network changes in the MEC. An increase of VGLUT1 was also detected in CA1 of young APP mice that stayed elevated across age (**Supplementary Figs. 22, 23a, c**). This finding explains the higher mean firing rate of adult APP place cells (**Fig. 2d**), and supports existing evidence showing that hyperexcitability is a major pathological symptom of AD[37]. Taken together, these results provide an in-depth overview of the early network changes in the MEC-hippocampal circuit susceptible to Aβ pathology at the molecular, physiological, and behavioral levels.

Discussion

To identify the impact of Aβ pathology on neural coding in the MEC-hippocampal circuit, we obtained single-unit recordings during the initial stages of disease in an APP mouse model of familial AD. These data revealed a disruption in entorhinal grid cell coding when initial Aβ fibrils are detected. In contrast, the spatial tuning of other functional cell types in the MEC and region CA1 of the hippocampus was preserved. Theta power and modulation of theta by running speed remained intact in adult APP mice, yet grid cells exhibited reduced theta rhythmicity and spatial stability. Grid cells in young and adult APP mice were decoupled from interneurons and head direction cells. These changes in grid cell coding corresponded with impaired performance of adult APP mice in a path integration task. Together, these results reveal that early Aβ pathology targets the entorhinal grid cell network within the MEC-hippocampal circuit.

Our results address several possible circuit-level explanations that could underlie reduced grid cell coding in APP mice. Prior studies have shown that inputs from the anterior thalamic nuclei (ATN), the dorsal hippocampus, and the medial septum are each independently necessary for normal grid cell function. Entorhinal head direction cells, which are dependent on direct and indirect inputs from the ATN[34], were preserved in adult APP mice, suggesting that projections from the ATN were intact. Place cells in the dorsal hippocampus remained spatially selective, stable, and had high firing rates, indicating that reduced feedback from the hippocampus cannot explain grid cell deficits in adult APP mice[28]. Finally, theta power and speed modulation of theta were preserved in adult APP mice, suggesting that medial septal theta-generating inputs to the MEC are conserved[25,26]. Nevertheless, our findings could still indicate a subtle impairment of basal forebrain inputs

that innervate the grid cell network; one candidate could be decreased septal cholinergic inputs[38], as a selective loss of basal forebrain cholinergic neurons in the nucleus basalis of Meynert is observed in familial AD patients[39,40].

We also observed that grid cells recorded in APP mice had reduced spike-timing synchrony with interneurons and head direction cells. This is interesting because interneuron mean firing rates and head direction directional selectivity were not lower in APP mice. These results are particularly significant because grid cells require excitatory, inhibitory and head direction inputs[28,32–34]. The decoupling of grid cells from interneurons and head direction cells therefore provides a network-level explanation for the reduced grid cell spatial periodicity and stability observed in adult APP mice. On that note, we could not analyze grid cell-place cell synchrony, given that we did not record from the MEC and CA1 simultaneously. This decoupling is also weakly present in young APP mice (as suggested by a two-way ANOVA, but insignificant via direct non-parametric testing), alluding to the possibility that grid cell coding is impaired prior to the complete loss of spatial periodicity. It could be that the decoupling effect is progressive and worsens with age, but we cannot directly confirm this idea with the current data and the lack of a significant effect size in young APP mice.

We also characterized whether local network-level changes can be accounted for at the molecular level. Based on our quantification of synaptic markers, VGLUT3 levels were pathologically elevated in the MEC of APP mice. These findings pinpoint specific inhibitory mechanisms as one of the earliest network changes in the MEC, as VGAT levels indicative of global inhibition were unaltered. However, these findings are hard to relate to the observed grid cell impairment. On the other hand, an increase of VGLUT1 was also detected in CA1 of young APP mice that stayed elevated across age. This finding explains the higher mean firing rates of

adult APP place cells and is consistent with the hypothesis that hyperexcitability is a major pathological symptom of AD[37]. We applied a linear mixed model and only considered marker expression levels that were significantly modulated by the subject's genotype. By doing so, a more subtle effect amongst other markers might have been deliberately missed. For instance, there was a slightly lower NR1 expression in adult APP mice relative to adult nTG mice, and it is known that this NMDA receptor subunit is necessary for grid cell firing[35].

Our results suggest that grid cells contribute to path integration, and possibly other forms of spatial memory. Young APP mice were modestly impaired in our path integration task despite an intact grid cell spatial periodicity. In parallel, prior work has shown spatial memory impairments in this APP mouse line at the same age in the radial arm and Morris water mazes[21,30]. An early disruption of the spike-timing relationship between grid cells and other MEC cell types in young APP mice could potentially underlie these behavioral impairments. Likewise, reduced grid cell spatial periodicity and stability could explain the pronounced path integration impairments in adult APP mice. Our behavioral data showed that in addition to increased travel distance and angular errors in the return path, adult APP mice spent more time along the environment periphery. This suggests that adult APP mice could not plan effective routes back to the refuge and instead adopted a thigmotaxic strategy. The severity of grid cell deficits paralleling the worsened behavioral performance provides compelling evidence to suggest that this microcircuit is linked to path integration and perhaps other forms of spatial memory. There are likely other undetermined factors that explain the spatial memory impairment observed in these mice at a young age, but our findings are consistent with the current understanding of how grid cells are necessary for proper path integration function[17,35].

Of particular importance, our results reveal that Aβ-mediated perturbations at the synaptic level do not uniformly impact neural computations. APP mice express soluble Aβ oligomers throughout the entorhinal cortex and exhibit a reduced density of presynaptic terminals and neuronal loss across all entorhinal layers by 6 months of age[20], yet only the grid cell subnetwork within the MEC was disrupted. Similar and widespread changes are observed throughout the hippocampus, but the spatial coding of place cells was not disrupted.

Place cells have also been recorded in other APP-related mouse models. The spatial tuning of place cells in the Tg2576 APP mouse model remained intact at the earliest incidence of Aβ plaques[27], similar to our results. However, differences in place cell physiology have also been reported. In the 3xTg triple transgenic mouse model displaying both APP and tau pathology, place cells exhibited spatial instability on a linear track preceding the detection of plaques which seems to be in conflict with our findings[41]. One explanation for this difference is environmental influence. As the mouse's freedom of movement is constrained on a one-dimensional track, the direction of instability is spatially restricted. In contrast, instability in an open field can occur in 360 degrees and averaging these directional shifts over time may ultimately cancel out to give the impression that APP place cells are stable. It could be that a linear track is more sensitive at detecting precise changes in place cell stability that may not meaningfully impact overall spatial coding in a two-dimensional environment. Alternatively, this difference could be due to the presence of tau pathology in 3xTg mice. In a different study involving a chimeric APP mouse model where the onset of APP expression could be controlled, place cell stability was also impaired on a linear track[42]. However, this disruption took place 9.5 months following APP expression, a pathogenic timepoint that is much later than ours which could explain their results. Lastly, a study reported that grid cells and place cells were disrupted in an

APP knock-in mouse model[43]. Despite already have moderate levels of plaque formation throughout the brain, these young APP knock-in mice still did not show any impaired place cell coding, which are consistent with our findings.

It is certain that inherent differences within mouse models may contribute to variability between results[41,42], but so can the experimental design. Our place cell results are best comparable to those recorded from Tg2576 mice[27] because recordings were done in an open field during the earliest detection of amyloid plaques. From this perspective, our results are consistent with what is currently known about Aβ pathology and place cell coding. To this growing body of knowledge, we show that impairments in grid cell firing emerge prior to place cell disruption. Importantly, both extracellular and intracellular Aβ-related processes may be pathogenic drivers of the reported network changes and should be further investigated. Despite the popular belief that extracellular Aβ initiates many aspects of pathology, there is a wide body of evidence showing that intracellular Aβ does the same[44–47].

Importantly, functional magnetic resonance imaging (fMRI) has revealed that the lateral entorhinal cortex (LEC) could be the first region affected in early AD[48]. The LEC is an important node in the entorhinal-hippocampal circuit and has also been studied in APP mouse models. In PDAPP mice, the location of amyloid deposits in the dentate gyrus greatly coincided with the termination of afferent projections from the LEC[49]. In terms of single-unit physiology, a report showed cells in Tg2576 mice displayed hyperactivity in the LEC by as early as 3 months of age[50]. Physiological changes in the LEC as a result of Aβ may precede the reported grid cell impairments and merit further investigation.

There is concern over the use of transgenic APP mouse models that overexpress non-physiological Aβ given the recent APP mutation knock-in mice which express pathological

profiles that are more faithful of AD pathogenesis. Here, we took advantage of the robust phenotypic nature of transgenic APP mice to identify the specific parts of the MEC-hippocampal spatial coding circuit most impacted by APP mutations. In parallel, AD is a multifaceted neurodegenerative disease marked by several mechanisms that contribute to impaired neural function. In particular, AD is characterized by widespread neurofibrillary tangles consisting of the hyperphosphorylated-tau protein. Prior work using a tau transgenic mouse line has shown that grid cell spatial coding is preserved when tau is initially restricted to axonal and somatodendritic compartments, but is subsequently impaired once tau has accumulated extensively in entorhinal cell bodies[51]. Our observations are consistent with reports on multi-study validation of data-driven disease progression in human AD patients[52,53]. The model predicts that cohorts of familial AD and *APOE*-ε4-positive subjects exhibit cerebrospinal fluid biomarkers in a distinct sequence: amyloid-β1–42, phosphorylated tau, and then total tau. However, in the broader AD population, total tau and phosphorylated tau are found to be earlier biomarkers than Aβ. The combined findings that early Aβ and advanced tau pathologies each independently target the grid cell network highlight the vulnerability of this entorhinal subnetwork and raise the possibility that spatial memory deficits in AD are linked directly to grid cell integrity. Indeed, functional imaging in young adults at genetic risk of AD (*APOE*-ε4 carriers) revealed a reduced grid-like hexa-symmetric signal in the MEC that correlated with spatial memory and path integration impairments[54–56]. These convergent lines of evidence support the viability of grid cell integrity and spatial navigation deficits as early markers of AD[4], and as dependent variables to assess the efficacy of AD therapeutics.

Methods

Subjects

J20 APP male mice (B6.Cg-Zbtb20 Tg(PDGFB-APPSwInd) 20Lms/2Mmjax) were obtained from Jackson Laboratories (MMRRC stock #34836) and bred with female C57/BL6/j mice. Mice were individually housed on a 12-h light/dark cycle and underwent experiments during the light cycle. All experimental procedures were performed in accordance with McGill University and Douglas Hospital Research Centre Animal Use and Care Committee (protocol #2015-7725) and in accordance with Canadian Institutes of Health Research guidelines.

In J20 mice, layers 2, 3 and 5 of the MEC undergo progressive neuronal loss and by 7.5 months of age, all layers experienced a combined loss of 16.3% in comparison to age-matched controls[18]. The entorhinal cortex as a whole exhibits a reduced density of presynaptic terminals (quantified by synaptophysin-immunoreactivity) by 7 months of age[20]. Similarly, by 6 months of age, region CA1 of the hippocampus in APP mice exhibits a 10%+ loss of neurons compared to age-matched controls[21]. Synapse loss is observed as early as 3 months of age in CA1, confirmed both by synaptic marker-immunoreactivity and electron microscopy[22]. In addition to these processes, the complement-dependent pathway and microglia undergo aberrant upregulation that is dependent on soluble Aβ oligomeric levels in the hippocampus[22]. Furthermore, gliosis (activated astrocytes) and neuroinflammation (activated microglia) become elevated across age in the hippocampus of 6-month-old APP mice[21]. Lastly, *in vitro* slice electrophysiology experiments revealed that both basal synaptic transmission recorded in CA1 and long-term potentiation in the Schaffer collateral–CA1 synapse are impaired in 3 month-old APP mice[23]. To examine the impact of these Aβ-

mediated changes on neural coding circuit during these early stages of Aβ pathology, we focused on APP mice between 3-7 months of age.

Single-unit recording data in the (MEC) were collected from 68 APP mice and littermates with negative transgene expression across four experimental groups: young APP mice (3-4.5 months of age), adult APP mice (4.5-7 months of age), young non-transgenic (nTG) mice (3-4.5 months of age), adult nTG mice (4.5-7 months of age). 31 males and 37 females were used. Some animals fell into multiple age groups. The male/female ratios were 5:5, 16:16, 4:7, and 9:10 for young APP, adult APP, young nTG, and adult nTG mice respectively. Single-unit recording data in region CA1 of the hippocampus were collected from six adult APP mice (3:3 male/female ratio) and six adult nTG mice (2:4 male/female ratio).

A separate, non-implanted cohort of APP and nTG mice were tested in the path integration behavior task. Mice were separated into the same four experimental groups defined above. The male/female ratios were 6:6, 6:3, 5:5, and 4:4 for young APP, adult APP, young nTG, and adult nTG mice respectively.

Surgery

On the day of surgery, mice were anesthetized with isoflurane (0.5% - 3% in O_2) and administered carprofen (0.01 ml/g) subcutaneously. For each mouse, three anchor screws were secured to the skull and a ground wire was positioned either above the cerebellum at midline position or the left visual cortex. A ‘versadrive’ containing four independently movable tetrodes (Axona, Inc) was implanted on top of the right MEC at the following stereotaxic coordinates: 3.4 mm lateral to the midline, 0.25-0.40 mm anterior to the transverse sinus. For hippocampal implants, the versadrive was implanted on top of the right CA1 at the following stereotaxic coordinates: 1.5 mm lateral to

the midline, 1.9 mm posterior from bregma. Tetrodes were gold-plated to lower impedances to 150-250 kΩ at 1 kHz prior to surgery. The versadrive was angled at eight degrees in the posterior direction for MEC implants and was not angled for CA1 implants. Following placement, the versadrive was secured in place using Kwik-Sil (to prevent exposure of the brain) and dental acrylic (to secure the versadrive to the skull and anchor screws). The ground wire was soldered to the implant, and tetrodes were lowered 1.0 mm and 0.5 mm from the dorsal surface for the MEC and CA1 respectively. All surgical procedures were performed in accordance with McGill University and Douglas Hospital Research Centre Animal Use and Care Committee (protocol #2015-7725) and in accordance with Canadian Institutes of Health Research guidelines.

Neural Recordings

Three days post-surgery, mice were placed on water restriction and maintained at 85% of their *ad libidum* weight for the duration of experiments. Mice were tested in six different open field environments. The majority of MEC recordings were done in a 75 x 75 cm box (1109 recordings), but a number of them also took place in a ten-sided maze with a 63.8 diameter (9 recordings), a 50 x 50cm box (121 recordings), a 84 x 84 cm box (23 recordings), a 90 x 90 cm box (1 recording), and a 100 x 100 cm box (58 recordings). All CA1 recordings were done in the same 75 x 75 cm box. As mice explored their environments, water droplets were randomly scatter throughout to motivate the subjects to adequately sample the entire open field. Once mice reliably provided good trajectory coverage, tetrodes were turned quickly until theta rhythmic units were observed which indicated that the tetrodes had entered the MEC. Tetrodes were then advanced in increments of 25 microns to sample new putative MEC neurons, which was later confirmed by histology. For the CA1 cohort, sleep recordings were carried out prior to open field exploration to detect sharp wave and ripple activity. Once ripple amplitude was stable across days, tetrodes were no longer turned.

Occasionally, tetrodes were either advanced or retracted depending on fluctuations in ripple amplitude and unit activity. In most cases for both MEC and CA1 recordings, neurons were not stable enough between recordings to reliably determine whether cells were re-sampled across days and thus we have included all cells recorded into our analysis.

To record spikes and local field potentials, versadrives were connected to a multichannel amplifier tethered to a digital Neuralynx (Bozeman, MT) recording system. Signals were amplified and band-pass filtered between 0.6 kHz and 6 kHz. Spike waveform thresholds were adjusted before commencing each recording and ranged between 35-140 µV depending on unit activity. Waveforms that crossed threshold were digitized at 32 kHz and recorded across all four channels of the given tetrode. Local field potentials were recorded across all tetrodes.

Histology

Animals were anesthetized with Isoflurane and perfused intracardially using saline, followed by 4% paraformaldehyde. Animal heads were left in 4% paraformaldehyde for between 24-72 hours following perfusion, before brains were extracted. Brains were left to sink in a 30% sucrose solution, and then frozen and stored in a -80ºC freezer. Sagittal brain sections (40µm) were sliced using a cryostat and Nissl-stained with a Cresyl violet solution. In cases where brain slices repeatedly came off the glass slides during Nissl-staining, slices were instead mounted using a fluorescent DAPI labeling mounting medium.

Tetrode tracks were characterized to be in either the superficial or deep layers based on the location of the track tip. Only data collected from tetrodes within the MEC were included in the analysis.

For hippocampal recordings, all tetrode tips that picked up single-units were determined to be in region CA1 of the dorsal hippocampus. Tips from tetrodes located outside of CA1 did not pick up any single-units.

Comparisons

Unit recording data was analyzed and compared across young and aged APP and nTG mice. All comparisons between baseline and other conditions used unpaired Wilcoxon rank sum tests with Bonferroni-Holm corrections for multiple comparisons with an alpha value of 0.05. Two-way unbalanced analysis of variance (ANOVA) tests were performed to detect any interaction effects between the subject's age and genotype on spatial tuning scores. Two-way unbalanced ANOVA tests were also performed to detect any interaction effects between the subject's genotype and cell type on spatial stability of grid, non-grid, and place cells. Analysis of co-variance (ANCOVA) tests were performed to compare speed modulation of theta power and theta frequency across groups. Wilcoxon rank sum tests with Bonferroni-Holm corrections for multiple comparisons with an alpha value of 0.05 were performed for all path integration behavioral and immunoautoradiographic analyses. Two-way unbalanced ANOVA tests were performed to detect any interaction effects between the subject's age and genotype on synaptic marker expression. The fitlme function in MATLAB was used to perform linear mixed effects analyses on the relationship between the subjects' genotype, age and synaptic marker expression. The fixed effects of the model comprised genotype and age (without interaction between the two). The random effects of the model comprised random intercepts by-subject, random slopes for the effects of genotype and age by-subject, and independence between the intercepts and slopes. P-values obtained in the model output were considered as the measurements for significance.

Spike sorting

Single-units were isolated 'offline' manually using graphical cluster cutting software (Plexon, Inc) individually for each recording session. Neurons were separated based on the peak amplitude and principal component measures of spike waveforms. Evaluation of the presence of biologically realistic interspike intervals, temporal autocorrelations, and cross correlations was used to confirm single-unit isolation. The experimenter was blind to the age and genotype of the subjects and only well-separated clusters were included in analysis.

Position, direction and velocity estimation

For all electrophysiological recordings, positional data was acquired at 30 frames per second at 720 x 480 pixel resolution (4.9 pixels per cm) using a camera purchased from Neuralynx (Bozeman, MT). The estimated position of the animal was calculated as the centroid of a group of red and green diodes positioned on the recording head stage. Head direction was calculated as the angle between the red and green diodes. Up to five lost samples due to occlusion of tracking LEDs, or reflections in the environment were replaced by a linear interpolation for both position and directional data. Running velocity was calculated using a Kalman filter. Rate maps were constructed by calculating the occupancy-normalized firing rate for 3cm x 3cm bins of position data. Data were smoothed by a two-dimensional convolution with a pseudo-Gaussian kernel involving a three pixel (9 cm) standard deviation. To visualize periodicity of grid fields, we computed the spatial autocorrelation of the smoothed rate maps using Pearson's product moment correlation coefficient as described in Supplementary Fig. 3.

Gridness score

To quantify the spatial periodicity of MEC neurons, we calculated a 'gridness score' as described in Brandon et al., 2011[25]. Briefly, this metric quantifies the hexagonal spatial periodicity in firing rate maps, while also accounting for elliptical eccentricity along one of two mirror lines that exist

in a hexagonal lattice structure. Distortion along one of the mirror lines was corrected after determining the major and minor axes of the grid based on the six fields closest to the central peak of the rate map autocorrelogram. The entire autocorrelogram was compressed along the major axis so that the major axis became equal to the minor axis. Large eccentricities (where the minor axis was less than half of the major axis) were not corrected. From the compressed autocorrelogram, we extracted a ring that encased the six peaks closest to the center peak but excluded the central peak to report periodicity between fields. We then calculated a rotational autocorrelation of this ring and observed the periodicity in paired pixel correlations across 180 degrees of rotation. The gridness score was computed as the difference between the lowest correlation observed at 60 or 120 degrees of rotation and the highest correlation observed at 30, 90, or 150 degrees of rotation. To ensure that our finding that grid cell reduction was not observed because of double-sampling grid cells across recording sessions, we made efforts to reduce putative double-sampling. Recordings of grid cells with cluster centroids within 0.2mV on subsequent days were considered to be putative duplicate recordings, and the grid cell recording with the best separation index was chosen for statistics on gridness across groups in Supplementary Fig. 7. We used the full set of recordings for all other analyses.

Directionality

Polar histograms of firing rate by head direction were generated to visualize the pattern of spiking dependent upon the animal's direction. To construct the polar plots, head direction was collected into bins of 6 degrees and the number of spikes in each bin was divided by the time spent facing that direction. The mean resultant length (MRL) of the polar plot was taken as a metric of head direction selectivity.

Cell selection

We categorized each entorhinal neuron as a grid cell, head direction cell, or non-grid spatially-tuned cell. We performed a shuffling procedure to set significance criteria to determine grid cells and head direction cells. Spike trains from each neuron recorded were randomly shifted in time by at least 30 seconds. We then calculated gridness and directionality measures. This process was repeated 50 times for each neuron, and the 99th percentile of the resulting distribution of scores was determined as the significance criteria for both measures. This results in a gridness threshold of 0.54 and directionality threshold of 0.21 which we used to define grid cells and head direction cells in our full dataset. Any cell recorded in the MEC which did not qualify as a grid cell but had a split-half correlation $\geq$ 0.6 was categorized as a non-grid spatially-tuned cell. Putative interneurons in the MEC were selected by having a narrow wave form (<0.3ms) and a mean firing rate of at least 0.5 Hz. Hippocampal neurons were classified as putative place cells if they had 1) a minimum mean firing rate of 0.1 Hz, 2) a maximum mean firing rate of 5.0 Hz, and 3) a spatial peak rate of greater than 5.0 Hz. Duplicate place cells sampled across recording sessions were removed for Fig. 2d and Fig. 3d.

Spatial 2D displacement analysis

To quantify noise in the two-dimensional (2D) phase of grid cells (and other cell types) on short timescales, we began by dividing the first 30 minutes of each recording into 10 epochs of three minutes each. For each epoch, we computed the resulting rate map. Next, for all pairwise comparisons of epoch rate maps, we computed the spatial cross-correlation between rate maps over a window of ±5 pixel (±15 cm) lags in both dimensions. The peak of this cross-correlogram captures the 2D translation necessary to best align the current pair of rate maps. Because the periodic nature of the grid pattern might lead to multiple local maxima in the cross-correlogram, we first computed the patch of correlation values nearest the center for which all contiguous

correlation values were at least 50% of the maximum correlation value. We then chose the maximum correlation in this patch as our peak. The distance from the center (no difference in alignment) to this peak was computed as our measure of 2D phase-shift between these epochs. The average across all pairwise comparisons of epochs was then the final measure of 2D phase noise for that cell.

Speed modulation of theta power and frequency

Local field potential traces obtained from the MEC were referenced to a cortical reference electrode and downsampled to 500 Hz. Power between 1-15Hz was calculated using a Morlett Wavelet with a 0.25 Hz bandwidth to obtain a power spectrum for each sample. Theta-by-Speed spectrograms were calculated as the power between 5-15 Hz divided by power in the delta band (2-4 Hz) across running speeds. The average Theta-by-Speed spectrogram is show in Fig. 2e. To quantify speed modulation of theta power, the mean power between 7-12 Hz across speeds was extracted from each Theta-by-Speed spectrogram across speeds (**Fig. 2e**). To quantify speed modulation of theta frequency, the frequency of the peak power for each running speed was extracted from the Theta-by-Speed spectrogram (**Fig. 2e**). Analysis of co-variance (ANCOVA) was performed on these extracted data.

Single-cell temporal autocorrelations and intrinsic frequency

The spike times of each cell were binned at 5ms intervals and the temporal autocorrelation for the given spike train was computed. The obtained signal was smoothed by a Gaussian kernel with 2 bin standard deviation, zero padded to 2^{13} samples and the power spectrum was calculated using the Chronux toolbox function MTSPECTRUMC from Matlab. The intrinsic frequency of a given cell was then taken as the frequency with the max power in the 6-12 Hz range.

Cross-correlations and synchrony analysis

To examine spiking synchrony unbiased cross-correlations were computed between simultaneously recorded grid cells, head direction cells, and putative interneurons with 5ms temporal bins from a lag of -400 to 400ms. The resulting cross-correlations were convolved with a 25ms gaussian and normalized to their median absolute deviation for comparison.

Path Integration Task

Data were collected in a ten-sided maze (diameter = 63.8 cm) surrounded by black curtains. Steel bars were screwed into the walls of the testing room and hovered over the maze. A plastic base was positioned on these bars and acting as the ceiling for the maze. On this ceiling, an infrared camera purchased from Neuralynx was positioned and acquired positional data at 30 frames per second at 720 x 480 pixel resolution (6.13 pixels per cm). Black curtains were positioned on top and around this plastic base which draped over the maze and ensured a complete darkness environment. Within the maze, 10 refuge enclosures connected to the open environment were closed off by top-down sliding doors that acted as walls. For all trials, the same refuge was used for each subject. When the door was slid open, the mouse could voluntarily enter or exit the refuge by their own volition. The height of these walls (and the entire maze throughout) was 27.6 cm.

Mice were placed on food restriction and maintained at 85% of their *ad libidum* weight throughout training and testing phases. In each trial, the mouse was kept in the same refuge enclosure separated from the open environment by the sliding door. The maze was operated in darkness via a pulley system which consisted of a rope fastened to the top of the sliding door. This rope extended outside of the curtains by passing through 2 clamps that were installed along the steel bars above the maze. This setup mimicked a pulley system where the experimenter could pull on the rope and open the sliding door while the curtains were draped over the maze. The handle of the rope end was twisted

into a knot; at the start of each trial, the rope was pulled, and the knot was looped onto a third clamp fastened to a table post. Doing so kept the sliding door held up throughout the duration of each trial. At the end of a trial, the knot was lifted from the clamp which closed the door. This setup allowed the experimenter to quickly operate the door without needing to physically interact with the maze.

Once the mouse was let into the open environment, it had to forage for a randomly placed small food pellet and return to the refuge prior to consumption. These food pellets were the same kind as administered in the subjects' cages, but smaller in size weighing less than 0.2 g. Successful trials were defined as events where the mouse picked up the food pellet and navigated to the refuge before consumption. Failed trials were defined as events where the mouse failed to return to its refuge before consuming the pellet. Incomplete trials were defined as events where the mouse failed to retrieve the pellet before returning to its refuge.

Visual cues were set up along the walls of the environment to allow for increased allocentric-guided behavior in the light trials. The three visual cues used consisted of a triangle, square, and three stripes constructed using tape and were positioned on three almost-equally spaced walls (given that the environment is ten-sided, a cue couldn't be completely equally-spaced from the other two). White noise played throughout all trials to account for potential auditory cues that may affect the mouse's return trajectory. Furthermore, the maze environment was wiped using Peroxyguard following every five consecutive trials to reduce the extent to which olfactory cues influenced behavior. In light trials, room lighting was turned on and the curtains were pushed to the side. In dark trials, room lighting was turned off and the curtains completely covered the arena. The mouse's movements were tracked using an overhead infrared camera, and the maze was lit using an infrared light.

Path Integration Behaviour Timecourse. Mice reached 85% of their *ad libidum* weight before experiments commenced. Mice first underwent a training phase where they achieved a minimum of eight successful trials out of ten total complete trials within a session in light conditions. Incomplete trials did not count as a completed trial. Mice went through consecutive light training days until they reached the success criteria. During failed trials, the experimenter punished the mouse by holding it by the tail suspended in air for ten seconds before placing it back into the refuge.

Following light training, mice then underwent five consecutive days of dark training. The same protocol as the light training applied to dark training. Mice were required to achieve a minimum of eight successful trials out of ten total complete trials within a session in any of the five days. All mice reported in the dataset achieved success criteria. Four mice that did not pass the training criteria were excluded from analysis. These mice included two young nTG mice, one young APP mouse, and one aged APP mouse.

Following dark training, mice then underwent five consecutive days of light and dark testing. In days 1, 3 and 5, five light trials were conducted, followed by five dark trials. Incomplete trials counted as trials. This was repeated until the mouse achieved ten complete trials in each of the light and dark conditions. On days 2 and 4, the same protocol applied, but the mouse started with five dark trials, followed by five light trials.

Analysis of Behavior Testing

All path integration behavioral data were recorded at 30 frames per second. The positional coordinates of the mice for each trial were obtained using an open-source deep learning tracker algorithm called DeepLabCut[57]. DeepLabCut was only used to quantify positional data in the path

integration task and not for electrophysiological recordings. Custom MATLAB scripts were used to analyze various behavioral parameters from the mice's positional data.

Genotyping

Tail samples were collected at weaning for genotyping, and just prior to brain perfusion for additional confirmation. DNA sample were extracted and amplified using the REDExtract-N-Amp™ Tissue PCR Kit (MilliporeSigma, XNAT-100RXN) and the primer sequence and PCR protocol provided by The Jackson Laboratory (MMRRC, 34836-JAX). Genotyping results were visualized using a QIAxcel instrument (Qiagen).

Immunofluorescence

Mice were anesthetized with Isoflurane (Baxter, FDG9623) and intracardially perfused with 0.05% heparin (Sandoz, 10750) in ice-cold saline followed up cold and filtered 4% paraformaldehyde that was freshly made from powder (MilliporeSigma, 158127-500g). Extracted brains were cryopreserved in 30% sucrose (MilliporeSigma, S0389-1Kg), flash frozen in 2-methylbutane (Fisher Scientific, 03551-4), and kept at -80ºC until sliced on a cryostat (Leica, CM3050-S). Sagittal sections (40µm) were collected on microscope slides for on-slide staining. Each slide had two positive controls (APP animals 18 months old) and at least one brain section from the remaining experimental groups (young APP, adult APP, young nTG, adult nTG). The same combinations of brain sections were used for both MEC and hippocampal staining. Sections that were too damaged were discarded. All slides were processed at the same time using the purified mouse monoclonal anti-beta-amyloid 1-16 antibody (6E10) (Biolegend, 803001) at 1/500 for 30 minutes, along with the M.O.M.® Fluorescein Kit (Vector Laboratories, FMK-2201). Slides were mounted with DAPI containing Fluoromount-G (SouthernBiotech, 0100-20).

691 ***Analysis of Immunofluorescence***

692 Images for each section were acquired within the same session at 10x magnification with the same
693 exposure settings (FITC: 250 ms, DAPI: 50 ms) on a slide scanner (Olympus, VS120) within one
694 week of the immunofluorescence assay. The images were digitally processed using ImageJ[47]. ROIs
695 were manually drawn for both MEC and the hippocampus and clear visually identifiable artifacts
696 were removed from ROIs. Rolling ball background subtraction (70µm radius) was applied to every
697 image. ROI areas were measured, and fluorescence intensity was extracted. A threshold was set
698 for analysis to capture the plaque fluorescence signal (6000 a.u.), based on beta amyloid plaques
699 observed in positive control animals. Using RStudio (RStudio Team 2016), the sections were
700 grouped by structure: MEC or hippocampus. For each animal, the normalized fluorescence was
701 calculated as the total fluorescence divided by the total area.

702 ***Immunoautoradiographic labelling of synaptic markers***

703 Immunoautoradiography experiments were performed on fresh frozen mouse brain sections
704 (10µm) as described previously[58,59]. Brain slices were taken at the level of the MEC (bregma 2.76
705 to 3.90) and the hippocampus (bregma -1.0 to -2.0). Slices were incubated overnight at 4° with
706 rabbit polyclonal antiserum specific of VGLUT1 (dilution 1:10,000), VGLUT3 (dilution 1:20,000,
707 Synaptic Systems, catalog number 135203, Göttingen Germany), VGAT (dilution 1:10,000,
708 Synaptic Systems, catalog number 131002, Göttingen Germany), VAChT (dilution 1:10,000,
709 Synaptic Systems, catalog number 139103, Göttingen Germany), NR1 (dilution 1:10,000,
710 Synaptic Systems, catalog number 114103, Göttingen Germany) and then with anti-rabbit [125I]-
711 IgG (PerkinElmer) for 2hr at 4°. Sections were then washed in PBS, rapidly rinsed in water, dried,
712 and exposed to x-ray films (Biomax MR, Kodak) for 5 days. Standard radioactive microscales
713 were exposed to each film to ensure that labeling densities were in the linear range. Densitometry

714 measurements were performed with MCID analysis software on sections for each region per mouse
715 (4 mice per experimental group for a total of 16 mice).

716 VGLUT1, VGLUT3, VACH and VGAT are vesicular transporters that mediate neurotransmission
717 from the presynaptic side. VGLUT1 is necessary for the vesicular accumulation of glutamate and
718 is a general marker for glutamatergic drive in synapses. In the context of grid cells, excitatory drive
719 is a prerequisite for grid cell generation[28]. VGLUT3 is a specific marker for synapses made by
720 CCK-positive basket cells in the MEC. VAChT expression in the MEC marks presynaptic
721 cholinergic terminals from the medial septum. The severe loss of cholinergic neurons is a hallmark
722 of Alzheimer's disease and a possible role of acetylcholine for grid cell activity has previously
723 been reported. VGAT mediates vesicular accumulation of GABA and is a general marker for
724 inhibitory drive which is important for grid cell generation[32,33]. In the case of NR1, it is a subunit
725 of NMDA receptors that has previously been shown to be necessary for both the generation of grid
726 cells and path integration ability[35].
727
728
729
730
731
732
733
734
735
736

References

1. Ferreira, S. T., Lourenco, M. V., Oliveira, M. M. & De Felice, F. G. Soluble amyloid-beta oligomers as synaptotoxins leading to cognitive impairment in Alzheimer's disease. *Front. Cell. Neurosci.* **9**, 191 (2015).
2. Alifragis, P. & Marsh, J. Synaptic dysfunction in Alzheimer's disease: the effects of amyloid beta on synaptic vesicle dynamics as a novel target for therapeutic intervention. *Neural Regen. Res.* **13**, 616 (2018).
3. Howett, D. *et al.* Differentiation of mild cognitive impairment using an entorhinal cortex-based test of virtual reality navigation. *Brain* **142**, 1751–1766 (2019).
4. Coughlan, G., Laczó, J., Hort, J., Minihane, A.-M. & Hornberger, M. Spatial navigation deficits - overlooked cognitive marker for preclinical Alzheimer disease? *Nat. Rev. Neurol.* **14**, 496–506 (2018).
5. Morris, R. G., Garrud, P., Rawlins, J. N. & O'Keefe, J. Place navigation impaired in rats with hippocampal lesions. *Nature* **297**, 681–683 (1982).
6. Smith, M. L. & Milner, B. The role of the right hippocampus in the recall of spatial location. *Neuropsychologia* **19**, 781–793 (1981).
7. Steffenach, H.-A., Witter, M., Moser, M.-B. & Moser, E. I. Spatial memory in the rat requires the dorsolateral band of the entorhinal cortex. *Neuron* **45**, 301–313 (2005).
8. O'Keefe, J. & Dostrovsky, J. The hippocampus as a spatial map. Preliminary evidence from unit activity in the freely-moving rat. *Brain Res.* **34**, 171–175 (1971).
9. Hafting, T., Fyhn, M., Molden, S., Moser, M.-B. & Moser, E. I. Microstructure of a spatial map in the entorhinal cortex. *Nature* **436**, 801–806 (2005).
10. Sargolini, F. *et al.* Conjunctive representation of position, direction, and velocity in entorhinal cortex. *Science* **312**, 758–762 (2006).
11. Ekstrom, A. D. *et al.* Cellular networks underlying human spatial navigation. *Nature* **425**, 184–188 (2003).
12. Jacobs, J. *et al.* Direct recordings of grid-like neuronal activity in human spatial navigation. *Nat. Neurosci.* **16**, 1188–1190 (2013).
13. Hasselmo, M. E., Hinman, J. R., Dannenberg, H. & Stern, C. E. Models of spatial and temporal dimensions of memory. *Curr. Opin. Behav. Sci.* **17**, 27–33 (2017).
14. O'Keefe, J. & Nadel, L. *The Hippocampus as a Cognitive Map*. (Oxford University Press, 1978).
15. Samsonovich, A. & McNaughton, B. L. Path integration and cognitive mapping in a continuous attractor neural network model. *J. Neurosci.* **17**, 5900–5920 (1997).
16. Burgess, N. & O'Keefe, J. Neuronal computations underlying the firing of place cells and their role in navigation. *Hippocampus* **6**, 749–762 (1996).
17. McNaughton, B. L., Battaglia, F. P., Jensen, O., Moser, E. I. & Moser, M.-B. Path integration and the neural basis of the "cognitive map." *Nat. Rev. Neurosci.* **7**, 663–678 (2006).
18. Mucke, L. *et al.* High-level neuronal expression of abeta 1-42 in wild-type human amyloid protein precursor transgenic mice: synaptotoxicity without plaque formation. *J. Neurosci.* **20**, 4050–4058 (2000).
19. Harris, J. A. *et al.* Transsynaptic progression of amyloid-β-induced neuronal dysfunction within the entorhinal-hippocampal network. *Neuron* **68**, 428–441 (2010).

20. Nagahara, A. H. *et al.* Early BDNF treatment ameliorates cell loss in the entorhinal cortex of APP transgenic mice. *J. Neurosci.* **33**, 15596–15602 (2013).
21. Wright, A. L. *et al.* Neuroinflammation and neuronal loss precede Aβ plaque deposition in the hAPP-J20 mouse model of Alzheimer's disease. *PLoS One* **8**, e59586 (2013).
22. Hong, S. *et al.* Complement and microglia mediate early synapse loss in Alzheimer mouse models. *Science* **352**, 712–716 (2016).
23. Saganich, M. J. *et al.* Deficits in synaptic transmission and learning in amyloid precursor protein (APP) transgenic mice require C-terminal cleavage of APP. *J. Neurosci.* **26**, 13428–13436 (2006).
24. Bjerknes, T. L., Dagslott, N. C., Moser, E. I. & Moser, M.-B. Path integration in place cells of developing rats. *Proc. Natl. Acad. Sci. U. S. A.* **115**, E1637–E1646 (2018).
25. Brandon, M. P. *et al.* Reduction of theta rhythm dissociates grid cell spatial periodicity from directional tuning. *Science* **332**, 595–599 (2011).
26. Koenig, J., Linder, A. N., Leutgeb, J. K. & Leutgeb, S. The spatial periodicity of grid cells is not sustained during reduced theta oscillations. *Science* **332**, 592–595 (2011).
27. Cacucci, F., Yi, M., Wills, T. J., Chapman, P. & O'Keefe, J. Place cell firing correlates with memory deficits and amyloid plaque burden in Tg2576 Alzheimer mouse model. *Proc. Natl. Acad. Sci. U. S. A.* **105**, 7863–7868 (2008).
28. Bonnevie, T. *et al.* Grid cells require excitatory drive from the hippocampus. *Nat. Neurosci.* **16**, 309–317 (2013).
29. Kropff, E., Carmichael, J. E., Moser, M.-B. & Moser, E. I. Speed cells in the medial entorhinal cortex. *Nature* **523**, 419–424 (2015).
30. Cheng, I. H. *et al.* Accelerating amyloid-beta fibrillization reduces oligomer levels and functional deficits in Alzheimer disease mouse models. *J. Biol. Chem.* **282**, 23818–23828 (2007).
31. Meilandt, W. J. *et al.* Neprilysin overexpression inhibits plaque formation but fails to reduce pathogenic Abeta oligomers and associated cognitive deficits in human amyloid precursor protein transgenic mice. *J. Neurosci.* **29**, 1977–1986 (2009).
32. Buetfering, C., Allen, K. & Monyer, H. Parvalbumin interneurons provide grid cell-driven recurrent inhibition in the medial entorhinal cortex. *Nat. Neurosci.* **17**, 710–718 (2014).
33. Miao, C., Cao, Q., Moser, M.-B. & Moser, E. I. Parvalbumin and somatostatin interneurons control different space-coding networks in the medial entorhinal cortex. *Cell* **171**, 507-521.e17 (2017).
34. Winter, S. S., Clark, B. J. & Taube, J. S. Spatial navigation. Disruption of the head direction cell network impairs the parahippocampal grid cell signal. *Science* **347**, 870–874 (2015).
35. Gil, M. *et al.* Impaired path integration in mice with disrupted grid cell firing. *Nat. Neurosci.* **21**, 81–91 (2018).
36. de Wilde, M. C., Overk, C. R., Sijben, J. W. & Masliah, E. Meta-analysis of synaptic pathology in Alzheimer's disease reveals selective molecular vesicular machinery vulnerability. *Alzheimers. Dement.* **12**, 633–644 (2016).
37. Palop, J. J. *et al.* Aberrant excitatory neuronal activity and compensatory remodeling of inhibitory hippocampal circuits in mouse models of Alzheimer's disease. *Neuron* **55**, 697–711 (2007).
38. Coyle, J. T., Price, D. L. & DeLong, M. R. Alzheimer's disease: a disorder of cortical cholinergic innervation. *Science* **219**, 1184–1190 (1983).

39. Whitehouse, P. J., Price, D. L., Clark, A. W., Coyle, J. T. & DeLong, M. R. Alzheimer disease: evidence for selective loss of cholinergic neurons in the nucleus basalis. *Ann. Neurol.* **10**, 122–126 (1981).
40. Liu, A. K. L., Chang, R. C.-C., Pearce, R. K. B. & Gentleman, S. M. Nucleus basalis of Meynert revisited: anatomy, history and differential involvement in Alzheimer's and Parkinson's disease. *Acta Neuropathol.* **129**, 527–540 (2015).
41. Mably, A. J., Gereke, B. J., Jones, D. T. & Colgin, L. L. Impairments in spatial representations and rhythmic coordination of place cells in the 3xTg mouse model of Alzheimer's disease. *Hippocampus* **27**, 378–392 (2017).
42. Zhao, R., Fowler, S. W., Chiang, A. C. A., Ji, D. & Jankowsky, J. L. Impairments in experience-dependent scaling and stability of hippocampal place fields limit spatial learning in a mouse model of Alzheimer's disease. *Hippocampus* **24**, 963–978 (2014).
43. Jun, H. *et al.* Disrupted place cell remapping and impaired grid cells in a knockin model of Alzheimer's disease. *Neuron* **107**, 1095-1112.e6 (2020).
44. LaFerla, F. M., Green, K. N. & Oddo, S. Intracellular amyloid-beta in Alzheimer's disease. *Nat. Rev. Neurosci.* **8**, 499–509 (2007).
45. Bayer, T. A. & Wirths, O. Intracellular accumulation of amyloid-Beta - a predictor for synaptic dysfunction and neuron loss in Alzheimer's disease. *Front. Aging Neurosci.* **2**, 8 (2010).
46. Saido, T. & Leissring, M. A. Proteolytic degradation of amyloid β-protein. *Cold Spring Harb. Perspect. Med.* **2**, a006379 (2012).
47. Leissring, M. A. & Turner, A. J. Regulation of distinct pools of amyloid β-protein by multiple cellular proteases. *Alzheimers. Res. Ther.* **5**, 37 (2013).
48. Khan, U. A. *et al.* Molecular drivers and cortical spread of lateral entorhinal cortex dysfunction in preclinical Alzheimer's disease. *Nat. Neurosci.* **17**, 304–311 (2014).
49. Reilly, J. F. *et al.* Amyloid deposition in the hippocampus and entorhinal cortex: quantitative analysis of a transgenic mouse model. *Proc. Natl. Acad. Sci. U. S. A.* **100**, 4837–4842 (2003).
50. Xu, W., Fitzgerald, S., Nixon, R. A., Levy, E. & Wilson, D. A. Early hyperactivity in lateral entorhinal cortex is associated with elevated levels of AβPP metabolites in the Tg2576 mouse model of Alzheimer's disease. *Exp. Neurol.* **264**, 82–91 (2015).
51. Fu, H. *et al.* Tau pathology induces excitatory neuron loss, grid cell dysfunction, and spatial memory deficits reminiscent of early Alzheimer's disease. *Neuron* **93**, 533-541.e5 (2017).
52. Archetti, D. *et al.* Multi-study validation of data-driven disease progression models to characterize evolution of biomarkers in Alzheimer's disease. *NeuroImage Clin.* **24**, 101954 (2019).
53. Young, A. L. *et al.* A data-driven model of biomarker changes in sporadic Alzheimer's disease. *Brain* **137**, 2564–2577 (2014).
54. Doeller, C. F., Barry, C. & Burgess, N. Evidence for grid cells in a human memory network. *Nature* **463**, 657–661 (2010).
55. Kunz, L. *et al.* Reduced grid-cell-like representations in adults at genetic risk for Alzheimer's disease. *Science* **350**, 430–433 (2015).
56. Bierbrauer, A. *et al.* Unmasking selective path integration deficits in Alzheimer's disease risk carriers. *Sci. Adv.* **6**, eaba1394 (2020).

57. Mathis, A. *et al.* DeepLabCut: markerless pose estimation of user-defined body parts with deep learning. *Nat. Neurosci.* **21**, 1281–1289 (2018).
58. Amilhon, B. *et al.* VGLUT3 (vesicular glutamate transporter type 3) contribution to the regulation of serotonergic transmission and anxiety. *J. Neurosci.* **30**, 2198–2210 (2010).
59. Vigneault, É. *et al.* Distribution of vesicular glutamate transporters in the human brain. *Front. Neuroanat.* **9**, 23 (2015).

Acknowledgments
We graciously thank S. Kim, Z. Ante, K. Harandian, Q. He, A. Ismailova, D. Patel, A. Zhen and A. Milette-Gagnon for technical assistance. We also thank J. Poirer, M. Hasselmo, J. Hinman, S. Villeneuve, S. Williams, R. Rozeske, J. Lee, J. Robinson and E. Vachon-Presseau for comments on earlier versions of this manuscript and to all members of the Brandon laboratory for helpful discussions.

Author contributions
J.Y. contributed to experimental design, recordings, analysis of data, and wrote the manuscript. R.L. contributed to immunohistochemistry quantifications. A.T.K contributed to analysis of data. E.V. and S.E.M contributed to immunoautoradiographic quantifications. M.P.B contributed to experimental design, analysis of data, and wrote the manuscript.

Competing interests
Authors declare no competing interests.

Materials & Correspondence
Correspondence to Mark P. Brandon.

Data availability
Source data for all experiments are publicly available at [insert Dryad link] or via request to the corresponding author.

Code availability
All custom codes written for reported analyses are publicly available at [insert GitHub link] or via request to the corresponding author.

Table 1. Summary of MEC cell yield within subject.

Animal ID#	Genotype	Sex	Age Group	# recording sessions	# total cells	# total cells MEC	# grid cells	# HD cells	# spatial cells
12015	nTG	F	A	5	21	18	0	7	0
12040	APP	M	A	11	35	35	1	5	1
12375	nTG	F	Y	21	114	114	1	35	14
12378	nTG	F	Y	9	28	28	1	12	0

12644	nTG	F	A	7	32	0	0	0	0
12646	APP	F	A	2	3	3	1	3	0
12655	nTG	F	A	5	15	4	0	2	0
12656	nTG	F	A	8	36	0	0	0	0
12746	nTG	F	A	10	36	36	2	20	3
12748	nTG	F	A	33	97	97	16	25	7
12756	nTG	F	A	10	36	8	0	3	4
12757	nTG	F	A	18	64	55	0	20	4
12758	APP	F	A	24	112	40	1	17	0
12759	APP	F	A	23	70	70	0	30	3
12784	APP	M	A	18	81	81	1	26	7
12785	APP	M	A	22	32	32	2	11	2
12786	nTG	M	A	18	60	60	1	9	7
12787	nTG	M	A	24	153	91	1	13	9
12788	APP	M	A	7	9	7	0	4	0
12790	APP	M	A	18	79	79	2	27	2
12791	nTG	M	A	38	192	192	1	49	17
12792	APP	M	A	14	31	31	1	11	1
12794	nTG	M	A	14	29	29	0	7	1
13530	APP	F	Y	10	29	5	0	3	0
13532	APP	F	Y	28	117	117	4	38	10
13534	APP	F	Y	30	142	142	27	21	31
13601	nTG	F	Y	18	67	7	0	0	0
13630	nTG	M	Y, A	33	260	260	79	45	29
13631	nTG	M	Y	16	95	95	0	38	6
13683	APP	F	A	12	64	64	1	17	3
13781	nTG	M	A	16	46	16	5	4	2
13782	nTG	M	A	26	168	168	31	54	20
13783	nTG	M	A	23	104	104	7	20	6
13784	nTG	M	A	14	65	11	1	2	1
13791	APP	F	A	14	43	43	0	5	0
13792	APP	F	A	13	40	40	0	5	2
13794	APP	F	Y	17	63	63	0	24	7
13795	APP	M	Y	21	91	64	0	15	3
13798	nTG	M	Y	19	106	106	7	16	10
13799	APP	M	Y	25	86	86	31	13	3
13827	nTG	M	Y	17	84	84	0	36	5
13828	APP	M	A	19	52	52	8	17	2
13884	nTG	F	Y, A	22	57	29	1	12	2

13885	nTG	F	Y, A	25	87	87	6	23	7
13894	APP	F	A	17	86	86	2	12	14
13895	nTG	F	Y	18	63	63	1	17	0
13927	APP	F	A	23	97	97	0	44	2
13928	nTG	F	Y	10	20	20	0	10	0
13931	APP	F	A	16	53	53	1	12	10
14012	APP	F	A	13	40	40	0	18	0
14014	APP	M	A	15	62	62	1	12	1
14015	APP	M	A	15	80	80	0	30	4
14020	APP	F	A	12	47	47	0	20	3
14117	APP	F	A	12	29	29	0	9	2
14118	APP	F	A	12	34	34	6	3	4
14125	APP	M	A	15	59	59	12	10	1
14574	APP	F	A	22	71	71	0	10	6
14593	APP	F	A	20	63	63	6	21	7
14598	APP	M	A	14	57	36	0	20	0
14599	APP	M	A	25	68	68	2	9	8
14623	APP	M	A	25	94	63	1	9	28
14754	APP	M	Y, A	30	175	139	1	31	5
14756	APP	M	Y, A	30	267	267	3	127	26
14757	APP	M	Y, A	34	168	164	8	43	7
14847	nTG	F	Y, A	21	63	63	0	25	1
14849	nTG	M	Y, A	20	95	52	1	16	1
15035	APP	F	Y, A	30	188	188	2	45	22
15036	nTG	F	Y	25	108	64	1	19	10

910 **Table 2. Summary of MEC cell yield within group.**

Group	# total cells	# grid cells	# HD cells	#spatial cells
APP-y	1032	74	306	106
nTG-y	998	64	295	82
APP-a	1665	50	471	119
nTG-a	964	99	244	83

911 **Table 3. Summary of CA1 cell yield within subject.**

Animal ID#	Genotype	Sex	# recording sessions	# total cells	# place cells
16129	APP	F	17	58	28
16130	nTG	F	15	74	58
16132	nTG	M	14	60	27
16133	APP	M	14	102	76
16135	nTG	M	24	137	79
16153	nTG	F	2	9	4

16154	APP	F	17	138	45
17624	APP	F	22	53	18
17625	nTG	F	18	87	37
17627	APP	F	19	115	51
17628	nTG	F	18	74	49
17903	APP	M	8	85	33

912 **Table 4. Summary of CA1 cell yield within group.**

Group	# total cells	# place cells
APP-a	551	251
nTG-a	441	254

913 **Table 5. Sample sizes of all statistical comparisons between groups in the main figures.**

Figure	nTG-y	nTG-a	J20-y	J20-a
1a-e	64	99	74	50
2a	295	244	306	471
2b	82	83	106	119
2c	n/a	118	n/a	109
2e	273	302	253	492
3a	64	98	74	50
3d – grid	61	95	73	49
3d – nongrid	82	83	106	119
3d - place	n/a	114	n/a	96
3e	61	95	73	49
4c – grid/int	60	115	34	54
4c – grid/HD	73	110	34	30
5d	377	307	500	301

914

915

916

917

918

919

920

921

922

923

924 **Figure Legend:**

925 **Fig. 1.** Reduction of grid cell spatial periodicity in adult APP transgenic mice. **a,** Firing rate maps
926 for grid cells from each experimental group. Each row includes 15 grid cells with the highest grid
927 scores sorted in descending order. The spatial peak firing rate and grid score are indicated in the
928 rate map's top-left and top-right, respectively. Non-transgenic young mice (nTG-y); non-
929 transgenic adult mice (nTG-a); APP young mice (APP-y); APP adult mice (APP-a). **b,** Cumulative
930 distribution function (CDF) compares the distribution of grid scores between experimental groups.
931 Inset bar graph displays the median and 3rd interquartile range (solid error bars). Y-axis of inset
932 bar graph indicates the grid score. (nTG-y vs. nTG-a: $p = 0.12$, nTG-y vs. APP-y: $p = 0.73$, APP-
933 y vs. APP-a: $p = 0.0000001$, nTG-a vs. APP-a: $p = 0.0000025$). **c,** Scatter plot displays grid score
934 by age recorded (in days). A two-way ANOVA was conducted to examine the effects of age and
935 genotype on grid score. There was a significant interaction between the effects of age and
936 genotype: $F(1, 280) = 11.99$, $p = 0.00062$. **d,** Color-coded rotational correlations are shown, sorted
937 in descending order of the grid score value. All neurons within the top 20% of grid scores are
938 shown. The max grid score in each experimental group is displayed at the top of the respective
939 plot. **e,** Same as (**b**), but panels compare spatial information, spatial peak firing rate, and mean
940 firing rate between groups. Inset bar graphs display the median and 3rd interquartile range (solid
941 error bars). (Spatial information: nTG-y vs. nTG-a: $p = 0.77$, nTG-y vs. APP-y: $p = 0.34$, APP-y
942 vs. APP-a: $p = 0.0000065$, nTG-a vs. APP-a: $p = 0.0012$; Spatial peak firing rate: nTG-y vs. nTG-
943 a: $p = 0.59$, nTG-y vs. APP-y: $p = 0.79$, APP-y vs. APP-a: $p = 0.77$, nTG-a vs. APP-a: $p = 0.27$;
944 Mean firing rate: nTG-y vs. nTG-a: $p = 0.99$, nTG-y vs. APP-y: $p = 0.086$, APP-y vs. APP-a: $p =$
945 0.13, nTG-a vs. APP-a: $p = 0.79$). Y-axes of all inset bar graphs indicate the value of the metric
946 being compared by the corresponding CDF plot. ** = $p<0.01$, *** = $p<0.001$, corrected for
947 multiple comparisons.

948

949 **Fig. 2.** Medial entorhinal head direction cells, non-grid spatially-tuned cells, CA1 place cells, and
950 medial entorhinal theta oscillations in adult APP mice. **a,** (Top) Polar plots of eight head-direction
951 cells for each group. Directional peak firing rate and mean resultant length (MRL) are indicated in
952 the top-left and top-right, respectively. (Bottom) CDF plots compare MRL, directional peak firing
953 rate, and mean firing rate of all head direction cells between experimental groups. Inset bar graphs
954 display the median and 3rd interquartile range (solid error bars). Y-axes of all inset bar graphs

indicate the value of the metric being compared by the corresponding CDF plot. (MRL: nTG-y vs. nTG-a: p = 0.051, nTG-y vs. APP-y: p = 0.45, APP-y vs. APP-a: p = 0.41, nTG-a vs. APP-a: p = 0.11; Spatial peak firing rate: nTG-y vs. nTG-a: p = 0.44, nTG-y vs. APP-y: p = 0.21, APP-y vs. APP-a: p = 0.96, nTG-a vs. APP-a: p = 0.073; Mean firing rate: nTG-y vs. nTG-a: p = 0.18, nTG-y vs. APP-y: p = 0.28, APP-y vs. APP-a: p = 0.87, nTG-a vs. APP-a: p = 0.08). **b,** (Top) Rate maps of eight non-grid spatially-tuned cells for each group. Spatial peak firing rate and split-half reliability scores are indicated in the top-left and top-right, respectively. (Bottom) Same as (**a**), but panels compare the average firing field size, spatial peak firing rate, and mean firing rate across groups. (Firing field size: nTG-y vs. nTG-a: p = 0.40, nTG-y vs. APP-y: p = 0.66, APP-y vs. APP-a: p = 0.64, nTG-a vs. APP-a: p = 0.37; Spatial peak firing rate: nTG-y vs. nTG-a: p = 0.028, nTG-y vs. APP-y: p = 0.49, APP-y vs. APP-a: p = 0.73, nTG-a vs. APP-a: p = 0.032; Mean firing rate: nTG-y vs. nTG-a: p = 0.76, nTG-y vs. APP-y: p = 0.37, APP-y vs. APP-a: p = 0.50, nTG-a vs. APP-a: p = 0.93). **c,** (Top) Rate maps of eight CA1 place cells in nTG and APP adult mice. (Bottom) Same as (**a**), but panels compare spatial information, spatial peak firing rate, and mean firing rate between adult nTG and adult APP mice. (Spatial information: nTG-a vs. APP-a: p = 0.08; Spatial peak firing rate: nTG-a vs. APP-a: p = 0.32; Mean firing rate: nTG-a vs. APP-a: p = 0.31). **d,** Comparison of spatial information and mean firing rates of CA1 place cells in adult nTG and APP mice when varying the cell selection criteria of peak spatial firing rate. The central mark of each bar is the median value of the metric being compared, the edges of each bar represent the 25th and 75th percentiles, and the solid lines extend to the most extreme values not considered outliers. The colored dots indicate the number of place cells that passed the selection threshold. **e,** (Left) Spectrograms compare the MEC theta frequency and power as a function of the animal's running speed. (Right) MEC theta power and frequency are independently displayed as a function of the animal's running speed. * = $p<0.05$.

Fig. 3. Grid cells in adult APP mice are spatially unstable. **a,** CDF plot compares the normalized firing field size of grid cells between groups. Inset bar graph displays the median and 3rd interquartile range (solid error bars). Y-axis of inset bar graph indicates the normalized firing field size. (nTG-y vs. nTG-a: p = 0.076, nTG-y vs. APP-y: p = 0.76, APP-y vs. APP-a: p = 0.52, nTG-a vs. APP-a: p = 0.0025). **b,** Each grid cell recording was split into 10 three minute partitions. Two dimensional spatial cross-correlations were computed across all partition pairs. Example cross-

correlations of the first partition to subsequent partitions in two grid cells recorded from a nTG and an APP mouse are shown to the right. **c,** (Left) Schematic shows that two dimensional spatial displacement was calculated as the distance between the peak correlation pixel and the center pixel of the cross-correlation. (Right) Two dimensional displacement of grid cells, non-grid spatially-tuned cells and place cells as a function of lags between partitions. Dots indicate mean values and arrow bars indicate standard error of mean. **d,** CDF plots compare the mean two dimensional displacement of grid cells, non-grid spatially-tuned cells and place cells between groups. Inset bar graphs display the median and 3rd interquartile range (solid error bars). Y-axes of all inset bar graphs indicate the mean two dimensional displacement. (Grid cells: nTG-y vs. nTG-a: $p = 0.76$, nTG-y vs. APP-y: $p = 0.76$, APP-y vs. APP-a: $p = 0.00091$, nTG-a vs. APP-a: $p = 0.00034$; Nongrid spatial cells: nTG-y vs. nTG-a: $p = 0.74$, nTG-y vs. APP-y: $p = 0.24$, APP-y vs. APP-a: $p = 0.19$, nTG-a vs. APP-a: $p = 0.87$; Place cells: nTG-a vs. APP-a: $p = 0.37$). **e,** CDF plot compares the mean two dimensional rotational displacement of one grid cell partition relative to another in the cross-correlation between groups. Inset bar graph displays the median and 3rd interquartile range (solid error bars). Y-axis of inset bar graph indicates the mean two dimensional rotational displacement. (nTG-y vs. nTG-a: $p = 0.15$, nTG-y vs. APP-y: $p = 0.87$, APP-y vs. APP-a: $p = 0.73$, nTG-a vs. APP-a: $p = 0.15$). *** = $p<0.001$, corrected for multiple comparisons.

Fig. 4. Reduced spike-time synchrony in grid cell-interneuron and grid cell-head direction cell pairs. **a,** Spike-time cross-correlations between grid cell-interneuron pairs (left) and grid cell-head direction cell pairs (right) for all experimental groups (rows). Each panel displays the normalized correlation (by median) by time lag (in ms). Black curves indicate median values and gray contours indicate median absolute deviation. Lighter gray columns indicate the 25 ms time window in each lag direction from 0 ms. **b,** Color-coded raster plots show the magnitude of co-activity within a 400 ms time window. Y-axes are sorted in descending order by cell-pairs with the maximum co-activity within a 25 ms time window, and numbers indicate the number of cell-pairs in each experimental group. **c,** Cumulative distribution functions (CDFs) compare the mean co-activity within a 25 ms time window between experimental groups for different cell-pair types. Inset bar graphs display the median and 3rd interquartile range (solid error bars). Y-axes of inset bar graphs indicate the mean co-activity within a 25 ms time window. (Grid-Interneuron: nTG-y vs. nTG-a: $p = 0.30$, nTG-y vs. APP-y: $p = 0.13$, APP-y vs. APP-a: $p = 0.51$, nTG-a vs. APP-a: $p = 0.0018$;

Grid-HD: nTG-y vs. nTG-a: p = 0.33, nTG-y vs. APP-y: p = 0.56, APP-y vs. APP-a: p = 0.078, nTG-a vs. APP-a: p = 0.038). * = p<0.05, *** = p<0.001. # = p = 0.078, corrected for multiple comparisons.

Fig. 5. Path integration is impaired in APP mice and worsens across age. **a,** Schematic of food-foraging task in total darkness. Mice left their refuge to forage for a randomly placed food pellet. Upon discovery, they navigated back to the refuge prior to consumption. **b,** (Left) The probability of reaching the refuge at the initial wall encounter is depicted in a polar plot. (Right) Probability density plot compares the likelihood of arriving at each of the ten walls between groups. W1 and W10 refer to the ten walls in consecutive order. **c,** Polar plots compare the probability of reaching the refuge at the initial wall encounter between groups. Probability values are indicated below polar plots for each group. **d,** CDF plots compare the initial wall angle, the initial heading angle, the normalized distance travelled and the proportion of the return path spent along the periphery between groups. Inset bar graphs display the median and 3rd interquartile range (solid error bars). Y-axes of all inset bar graphs indicate the value of the metric being compared by the corresponding CDF plot. The calculation of each metric is shown in schematics above their respective plots. (Initial wall angle: nTG-y vs. nTG-a: p = 0.50, nTG-y vs. APP-y: p = 6.3e-15, APP-y vs. APP-a: p = 0.11, nTG-a vs. APP-a: p = 5.6e-15; Initial heading angle: nTG-y vs. nTG-a: p = 0.22, nTG-y vs. APP-y: p = 3.1e-10, APP-y vs. APP-a: p = 1.9e-5, nTG-a vs. APP-a: p = 9.5e-17; Normalized distance travelled: nTG-y vs. nTG-a: p = 0.0083, nTG-y vs. APP-y: p = 1.2e-6, APP-y vs. APP-a: p = 1.2e-6, nTG-a vs. APP-a: p = 3.9e-11; Proportion of path along walls: nTG-y vs. nTG-a: p = 0.74, nTG-y vs. APP-y: p = 0.011, APP-y vs. APP-a: p = 7.1e-5, nTG-a vs. APP-a: p = 1.6e-7). ** = p<0.01, *** = p<0.001, corrected for multiple comparisons. **e,** Bar graphs compare the relative percent increase of the initial wall angle, the initial heading angle, the normalized distance travelled and the proportion of the return path spent along the periphery between groups. Each bar consists of adult group values that were normalized against the mean value of their young genotype-matched counterparts. Bars indicate the mean and error bars indicate standard error of means. (Initial wall angle: p = 0.031; Initial heading angle: p = 0.00011; Normalized distance travelled: p = 0.031; Proportion of path along walls: p = 0.00032). * = p<0.05, *** = p<0.001.

Figure 1 - Ying

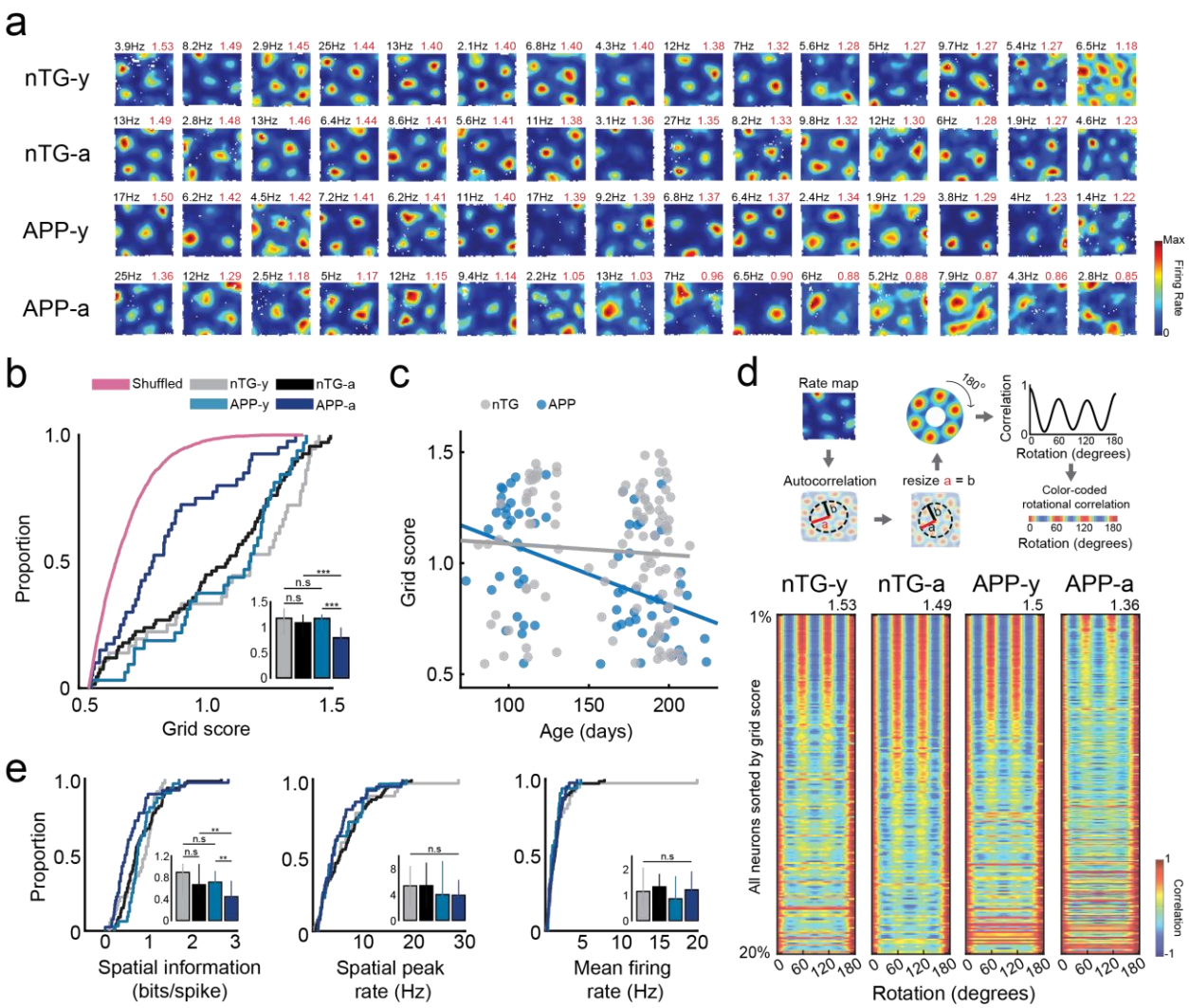

Fig. 1. Reduction of grid cell spatial periodicity in adult APP transgenic mice. **a**, Firing rate maps for grid cells from each experimental group. Each row includes 15 grid cells with the highest grid scores sorted in descending order. The spatial peak firing rate and grid score are indicated in the rate map's top-left and top-right, respectively. Non-transgenic young mice (nTG-y); non-transgenic adult mice (nTG-a); APP young mice (APP-y); APP adult mice (APP-a). **b**, Cumulative distribution function (CDF) compares the distribution of grid scores between experimental groups. Inset bar graph displays the median and 3rd interquartile range (solid error bars). Y-axis of inset bar graph indicates the grid score. (nTG-y vs. nTG-a: p = 0.12, nTG-y vs. APP-y: p = 0.73, APP-y vs. APP-a: p = 0.0000001, nTG-a vs. APP-a: p = 0.0000025). **c**, Scatter plot displays grid score by age recorded (in days). A two-way ANOVA was conducted to examine the effects of age and genotype on grid score. There was a significant interaction between the effects of age and genotype: F (1, 280) = 11.99, p = 0.00062. **d**, Color-coded rotational correlations are shown, sorted in descending order of the grid score value. All neurons within the top 20% of grid scores are shown. The max grid score in each experimental group is displayed at the top of the respective plot. **e**, Same as (**b**), but panels compare spatial information, spatial peak firing rate, and mean firing rate between groups. Inset bar graphs display the median and 3rd interquartile range (solid error bars). (Spatial information: nTG-y vs. nTG-a: p = 0.77, nTG-y vs. APP-y: p = 0.34, APP-y vs. APP-a: p = 0.0000065, nTG-a vs. APP-a: p = 0.0012; Spatial peak firing rate: nTG-y vs. nTG-a: p = 0.59, nTG-y vs. APP-y: p = 0.79, APP-y vs. APP-a: p = 0.77, nTG-a vs. APP-a: p = 0.27; Mean firing rate: nTG-y vs. nTG-a: p = 0.99, nTG-y vs. APP-y: p = 0.086, APP-y vs. APP-a: p = 0.13, nTG-a vs. APP-a: p = 0.79). Y-axes of all inset bar graphs indicate the value of the metric being compared by the corresponding CDF plot. ** = p<0.01, *** = p<0.001, corrected for multiple comparisons.

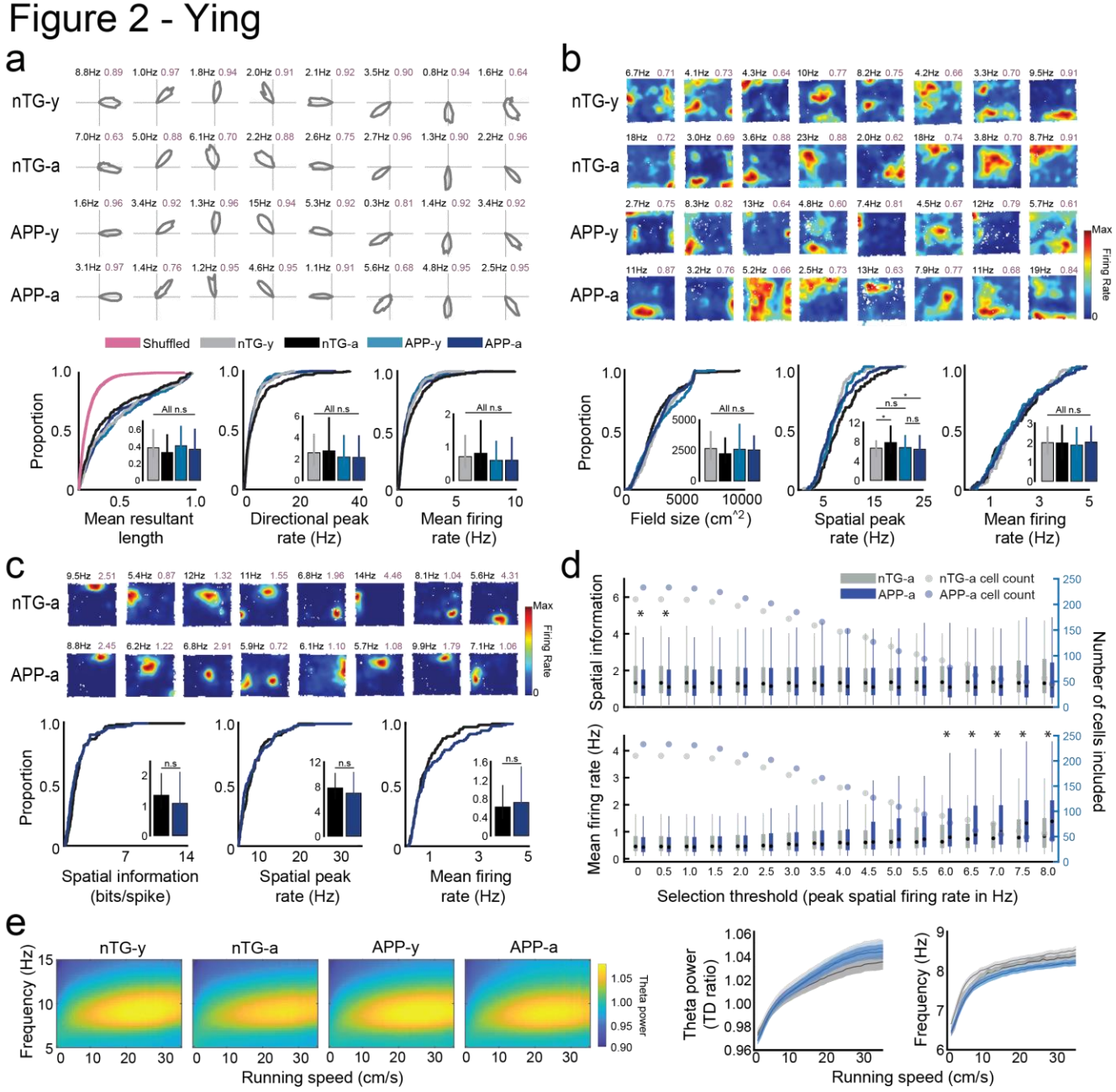

Fig. 2. Medial entorhinal head direction cells, non-grid spatially-tuned cells, CA1 place cells, and medial entorhinal theta oscillations in adult APP mice. **a**, (Top) Polar plots of eight head-direction cells for each group. Directional peak firing rate and mean resultant length (MRL) are indicated in the top-left and top-right, respectively. (Bottom) CDF plots compare MRL, directional peak firing rate, and mean firing rate of all head direction cells between experimental groups. Inset bar graphs display the median and 3rd interquartile range (solid error bars). Y-axes of all inset bar graphs indicate the value of the metric being compared by the corresponding CDF plot. (MRL: nTG-y vs. nTG-a: p = 0.051, nTG-y vs. APP-y: p = 0.45, APP-y vs. APP-a: p = 0.41, nTG-a vs. APP-a: p = 0.11; Spatial peak firing rate: nTG-y vs. nTG-a: p = 0.44, nTG-y vs. APP-y: p = 0.21, APP-y vs. APP-a: p = 0.96, nTG-a vs. APP-a: p = 0.073; Mean firing rate: nTG-y vs. nTG-a: p = 0.18, nTG-y vs. APP-y: p = 0.28, APP-y vs. APP-a: p = 0.87, nTG-a vs. APP-a: p = 0.08). **b**, (Top) Rate maps of eight non-grid spatially-tuned cells for each group. Spatial peak firing rate and split-half reliability scores are indicated in the top-left and top-right, respectively. (Bottom) Same as (**a**), but panels compare the average firing field size, spatial peak firing rate, and mean firing rate across groups. (Firing field size: nTG-y vs. nTG-a: p = 0.40, nTG-y vs. APP-y: p = 0.66, APP-y vs. APP-a: p = 0.64, nTG-a vs. APP-a: p = 0.37; Spatial peak firing rate: nTG-y vs. nTG-a: p = 0.028, nTG-y vs. APP-y: p = 0.49, APP-y vs. APP-a: p = 0.73, nTG-a vs. APP-a: p = 0.032; Mean firing rate: nTG-y vs. nTG-a: p = 0.76, nTG-y vs. APP-y: p = 0.37, APP-y vs. APP-a: p = 0.50, nTG-a vs. APP-a: p = 0.93). **c**, (Top) Rate maps of eight CA1 place cells in nTG and APP adult mice. (Bottom) Same as (**a**), but panels compare spatial information, spatial peak firing rate, and mean firing rate between adult nTG and adult APP mice. (Spatial information: nTG-a vs. APP-a: p = 0.08; Spatial peak firing rate: nTG-a vs. APP-a: p = 0.32; Mean firing rate: nTG-a vs. APP-a: p = 0.31). **d**, Comparison of spatial information and mean firing rates of CA1 place cells in adult nTG and APP mice when varying the cell selection criteria of peak spatial firing rate. The central mark of each bar is the median value of the metric being compared, the edges of each bar represent the 25th and 75th percentiles, and the solid lines extend to the most extreme values not considered outliers. The colored dots indicate the number of place cells that passed the selection threshold. **e**, (Left) Spectrograms compare the MEC theta frequency and power as a function of the animal's running speed. (Right) MEC theta power and frequency are independently displayed as a function of the animal's running speed. * = p<0.05.

Figure 3 - Ying

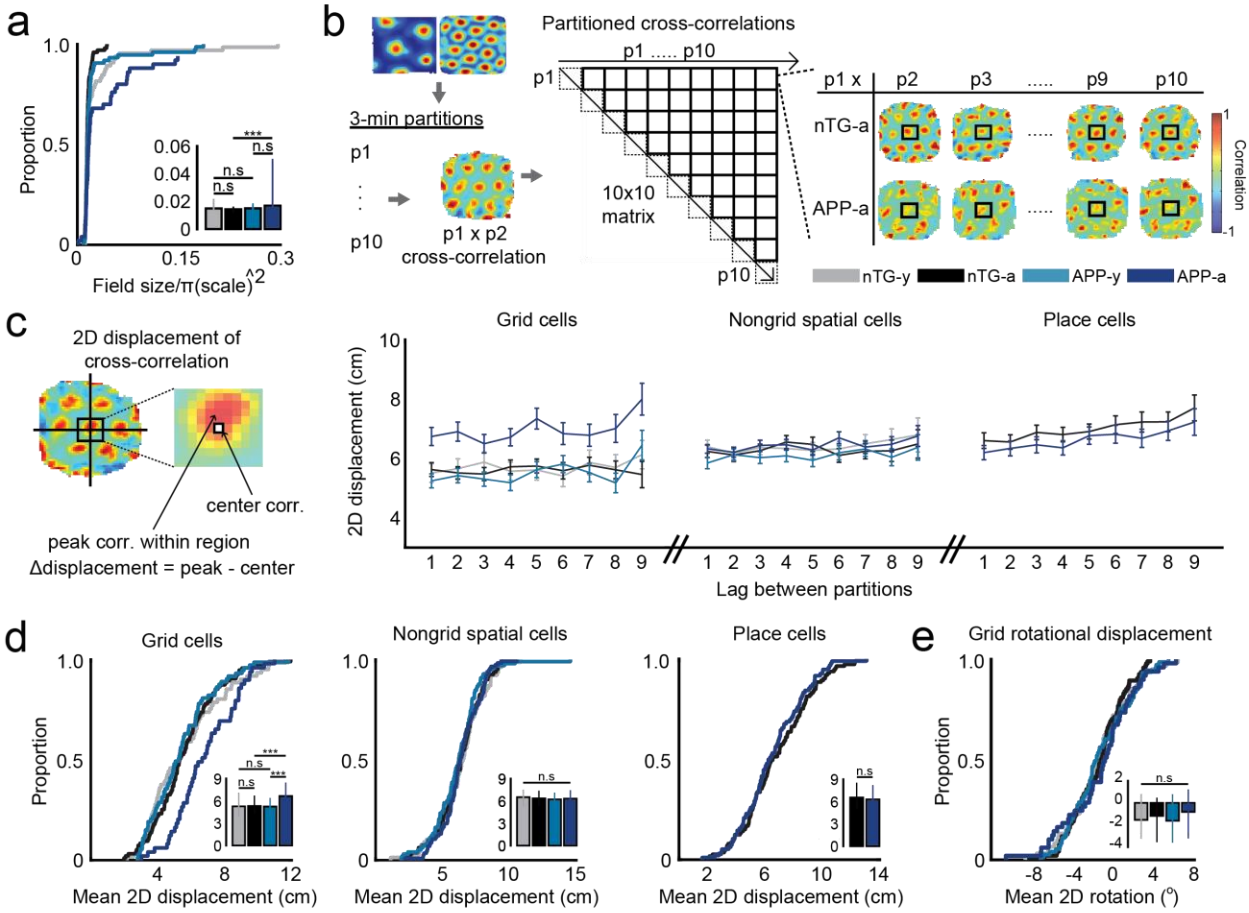

Fig. 3. Grid cells in adult APP mice are spatially unstable. **a**, CDF plot compares the normalized firing field size of grid cells between groups. Inset bar graph displays the median and 3rd interquartile range (solid error bars). Y-axis of inset bar graph indicates the normalized firing field size. (nTG-y vs. nTG-a: p = 0.076, nTG-y vs. APP-y: p = 0.76, APP-y vs. APP-a: p = 0.52, nTG-a vs. APP-a: p = 0.0025). **b**, Each grid cell recording was split into 10 three minute partitions. Two dimensional spatial cross-correlations were computed across all partition pairs. Example cross-correlations of the first partition to subsequent partitions in two grid cells recorded from a nTG and an APP mouse are shown to the right. **c**, (Left) Schematic shows that two dimensional spatial displacement was calculated as the distance between the peak correlation pixel and the center pixel of the cross-correlation. (Right) Two dimensional displacement of grid cells, non-grid spatially-tuned cells and place cells as a function of lags between partitions. Dots indicate mean values and arrow bars indicate standard error of mean. **d**, CDF plots compare the mean two dimensional displacement of grid cells, non-grid spatially-tuned cells and place cells between groups. Inset bar graphs display the median and 3rd interquartile range (solid error bars). Y-axes of all inset bar graphs indicate the mean two dimensional displacement. (Grid cells: nTG-y vs. nTG-a: p = 0.76, nTG-y vs. APP-y: p = 0.76, APP-y vs. APP-a: p = 0.00091, nTG-a vs. APP-a: p = 0.00034; Nongrid spatial cells: nTG-y vs. nTG-a: p = 0.74, nTG-y vs. APP-y: p = 0.24, APP-y vs. APP-a: p = 0.19, nTG-a vs. APP-a: p = 0.87; Place cells: nTG-a vs. APP-a: p = 0.37). **e**, CDF plot compares the mean two dimensional rotational displacement of one grid cell partition relative to another in the cross-correlation between groups. Inset bar graph displays the median and 3rd interquartile range (solid error bars). Y-axis of inset bar graph indicates the mean two dimensional rotational displacement. (nTG-y vs. nTG-a: p = 0.15, nTG-y vs. APP-y: p = 0.87, APP-y vs. APP-a: p = 0.73, nTG-a vs. APP-a: p = 0.15). *** = p<0.001, corrected for multiple comparisons.

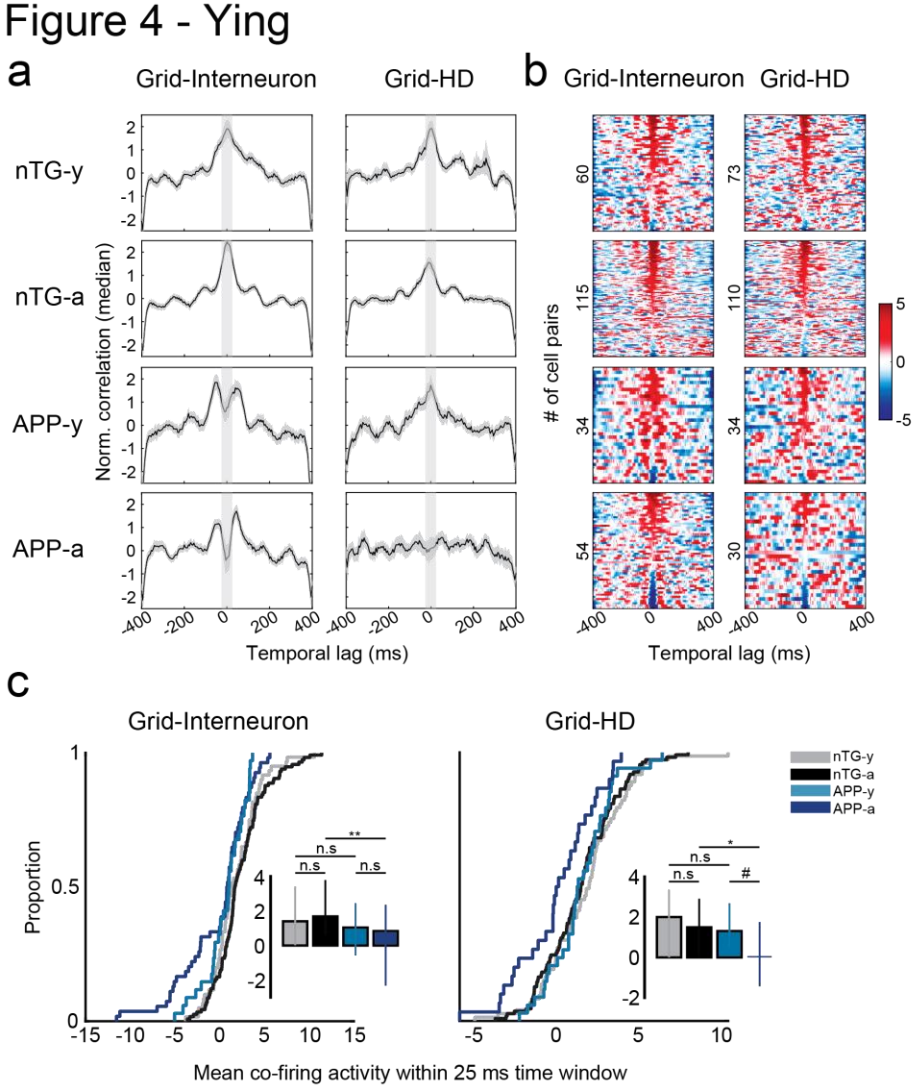

Fig. 4. Reduced spike-time synchrony in grid cell-interneuron and grid cell-head direction cell pairs. **a,** Spike-time cross-correlations between grid cell-interneuron pairs (left) and grid cell-head direction cell pairs (right) for all experimental groups (rows). Each panel displays the normalized correlation (by median) by time lag (in ms). Black curves indicate median values and gray contours indicate median absolute deviation. Lighter gray columns indicate the 25 ms time window in each lag direction from 0 ms. **b,** Color-coded raster plots show the magnitude of co-activity within a 400 ms time window. Y-axes are sorted in descending order by cell-pairs with the maximum co-activity within a 25 ms time window, and numbers indicate the number of cell-pairs in each experimental group. **c,** Cumulative distribution functions (CDFs) compare the mean co-activity within a 25 ms time window between experimental groups for different cell-pair types. Inset bar graphs display the median and 3rd interquartile range (solid error bars). Y-axes of inset bar graphs indicate the mean co-activity within a 25 ms time window. (Grid-Interneuron: nTG-y vs. nTG-a: p = 0.30, nTG-y vs. APP-y: p = 0.13, APP-y vs. APP-a: p = 0.51, nTG-a vs. APP-a: p = 0.0018; Grid-HD: nTG-y vs. nTG-a: p = 0.33, nTG-y vs. APP-y: p = 0.56, APP-y vs. APP-a: p = 0.078, nTG-a vs. APP-a: p = 0.038). * = p<0.05, *** = p<0.001. # = p = 0.078, corrected for multiple comparisons.

Figure 5 - Ying

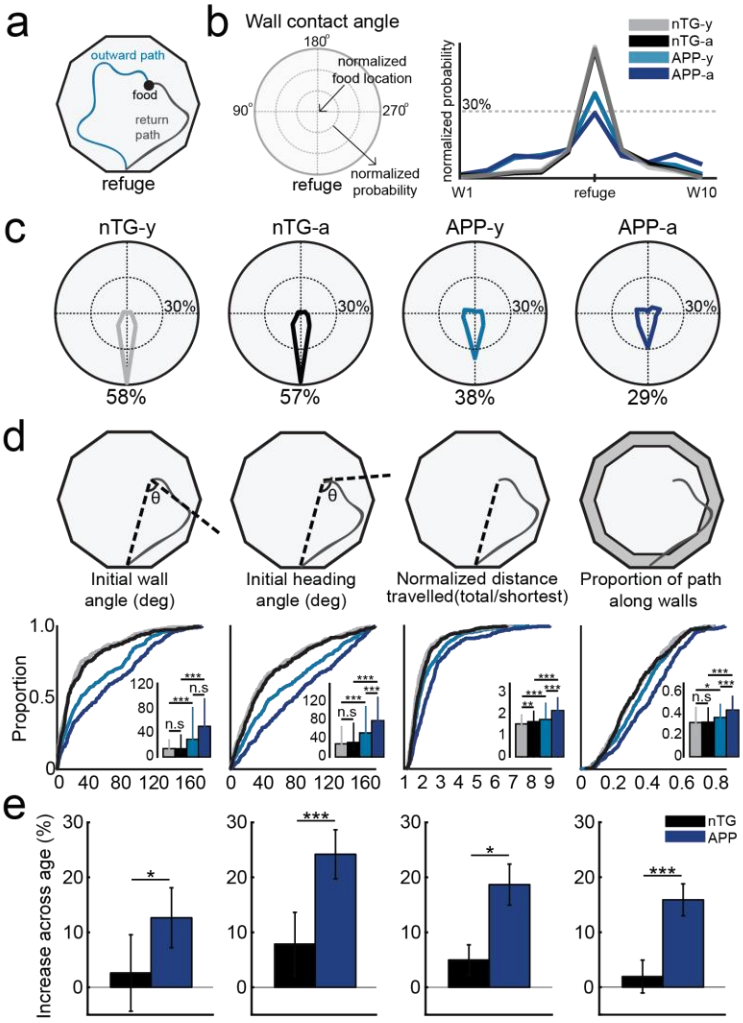

Fig. 5. Path integration is impaired in APP mice and worsens across age. **a**, Schematic of food-foraging task in total darkness. Mice left their refuge to forage for a randomly placed food pellet. Upon discovery, they navigated back to the refuge prior to consumption. **b**, (Left) The probability of reaching the refuge at the initial wall encounter is depicted in a polar plot. (Right) Probability density plot compares the likelihood of arriving at each of the ten walls between groups. W1 and W10 refer to the ten walls in consecutive order. **c**, Polar plots compare the probability of reaching the refuge at the initial wall encounter between groups. Probability values are indicated below polar plots for each group. **d**, CDF plots compare the initial wall angle, the initial heading angle, the normalized distance travelled and the proportion of the return path spent along the periphery between groups. Inset bar graphs display the median and 3rd interquartile range (solid error bars). Y-axes of all inset bar graphs indicate the value of the metric being compared by the corresponding CDF plot. The calculation of each metric is shown in schematics above their respective plots. (Initial wall angle: nTG-y vs. nTG-a: p = 0.50, nTG-y vs. APP-y: p = 6.3e-15, APP-y vs. APP-a: p = 0.11, nTG-a vs. APP-a: p = 5.6e-15; Initial heading angle: nTG-y vs. nTG-a: p = 0.22, nTG-y vs. APP-y: p = 3.1e-10, APP-y vs. APP-a: p = 1.9e-5, nTG-a vs. APP-a: p = 9.5e-17; Normalized distance travelled: nTG-y vs. nTG-a: p = 0.0083, nTG-y vs. APP-y: p = 1.2e-6, APP-y vs. APP-a: p = 1.2e-6, nTG-a vs. APP-a: p = 3.9e-11; Proportion of path along walls: nTG-y vs. nTG-a: p = 0.74, nTG-y vs. APP-y: p = 0.011, APP-y vs. APP-a: p = 7.1e-5, nTG-a vs. APP-a: p = 1.6e-7). ** = p<0.01, *** = p<0.001, corrected for multiple comparisons. **e**, Bar graphs compare the relative percent increase of the initial wall angle, the initial heading angle, the normalized distance travelled and the proportion of the return path spent along the periphery between groups. Each bar consists of adult group values that were normalized against the mean value of their young genotype-matched counterparts. Bars indicate the mean and error bars indicate standard error of means. (Initial wall angle: p = 0.031; Initial heading angle: p = 0.00011; Normalized distance travelled: p = 0.031; Proportion of path along walls: p = 0.00032). * = p<0.05, *** = p<0.001.

Supplementary Figures for:

Disruption of the grid cell network in a mouse model of early Alzheimer's disease

Supplementary Figure 1

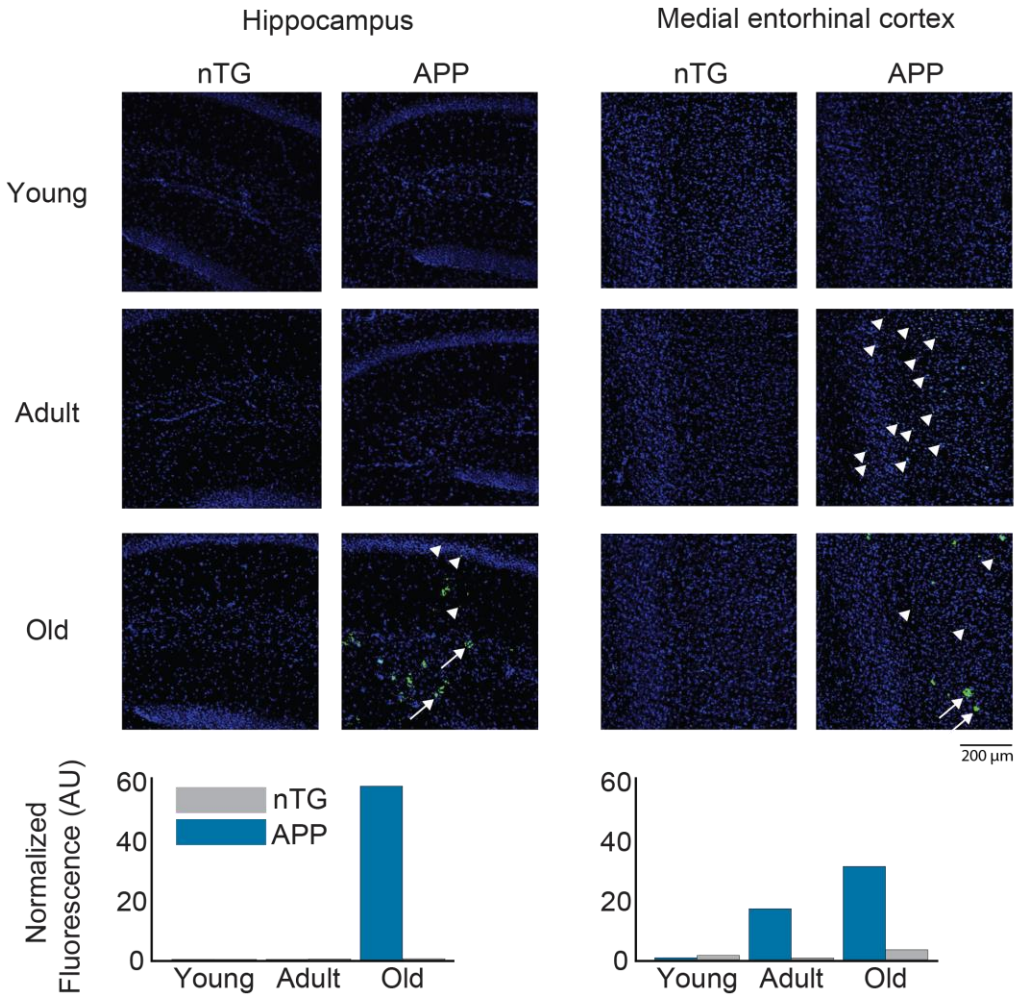

Supplementary Figure 1. Quantification of amyloid-beta plaques in APP mice. Representative examples of magnified brain sections of the hippocampus and medial entorhinal cortex of nTG and APP mice across 3 different age groups: young (3-4.5 mo.), adult (4.5-7 mo.) and old (18 mo.). Arrows and arrowheads indicate the presence of two different kinds of fluorescent morphologies. Adult APP mice have low levels of fluorescence in the medial entorhinal cortex, but the fluorescent signal is intracellular and does not resemble the bigger and widespread morphology observed in the hippocampus and medial entorhinal cortex of old APP mice. The fluorescence signal in adult APP mice might therefore represent early deposition of fibrillar amyloid-beta prior to the formation of mature plaques.

Supplementary Figure 2. Page 1

Supplementary Figure 2. Page 2

c

nTG-y

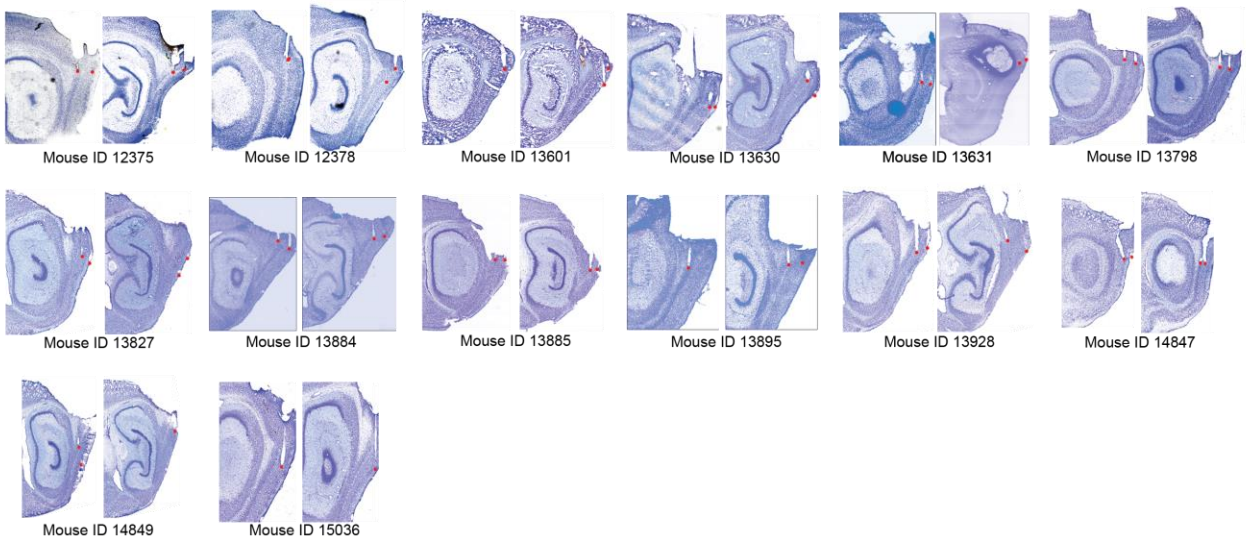

nTG-a

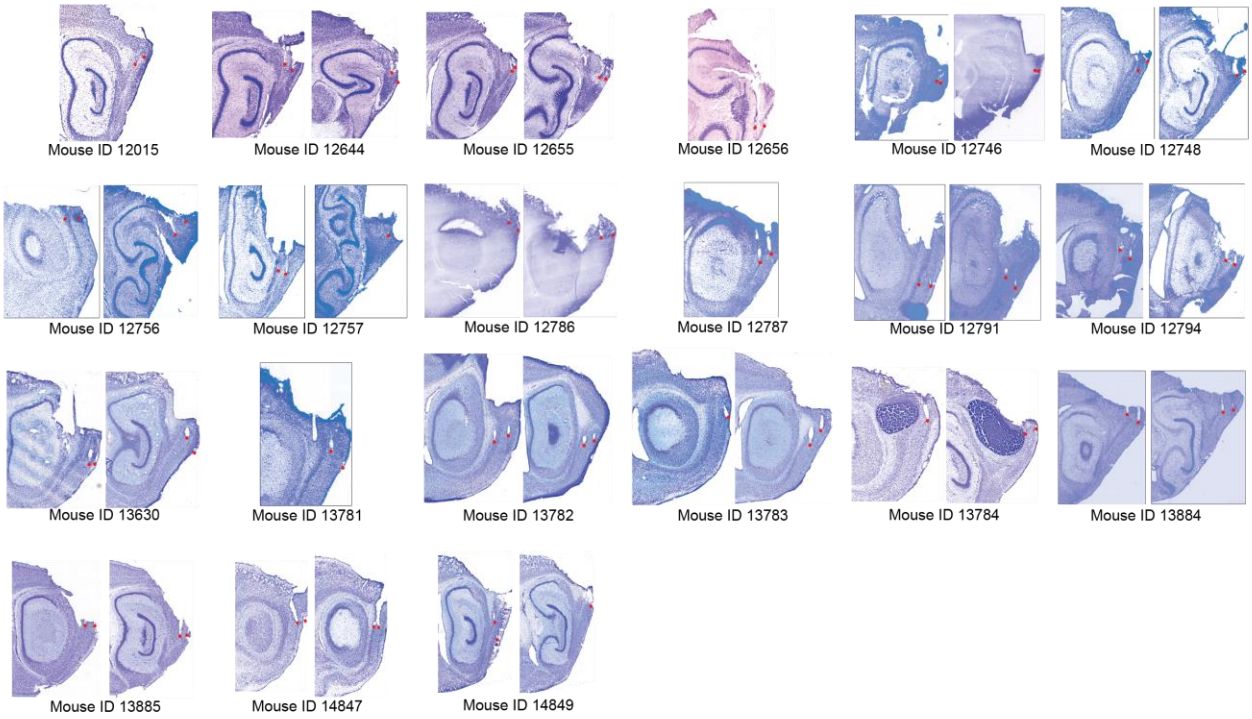

Supplementary Figure 2. Page 3

Supplementary Figure 2. Tetrode track histology for MEC recordings. **a**, Averaged sagittal brain sections from the most lateral part of MEC (far right) to the start of parasubiculum (far left). The individual track locations obtained from each animal were plotted along these sections by experimental group. **b**, Quantification of track locations shown in (**a**). (Left) Comparison of the percentage of tetrode tips located in the MEC between groups. (Right) Comparison of the percentage of tetrode tip in either the superficial or deep layers of MEC between groups. **c**, Track locations of each animal ordered by genotype and age. The tips of tracks are highlighted with a red dot.

Supplementary Figure 3

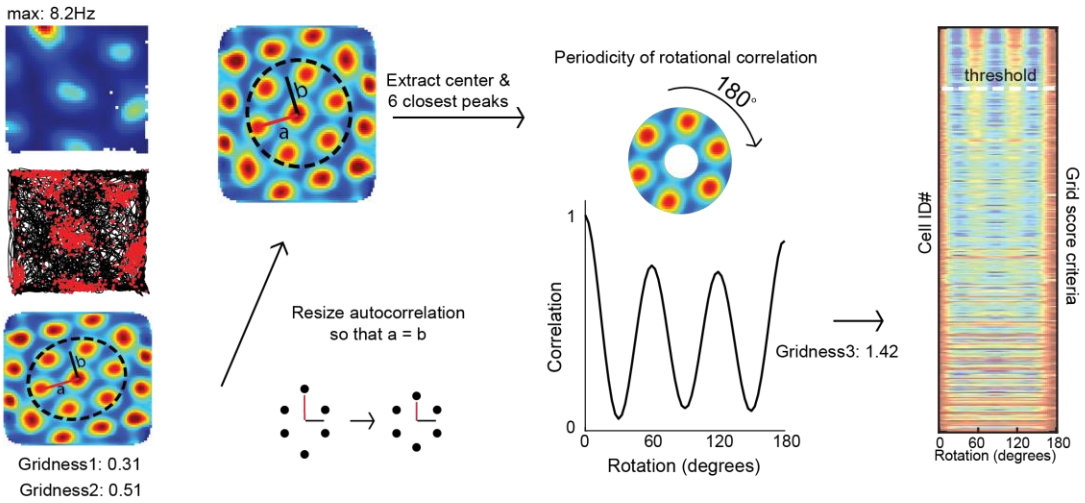

Supplementary Figure 3. Creation of raster plots indicating the strength of rotational correlation of each cell. Autocorrelations of grid cell rate maps were resized to ensure that the major and minor axes, a and b, were equal in length. The resulting image was then rotated 180 degrees to compute a color-coded row indicating the correlation strength at each degree of rotation. These rows were then sorted by decreasing order of grid score in a raster plot.

Supplementary Figure 4

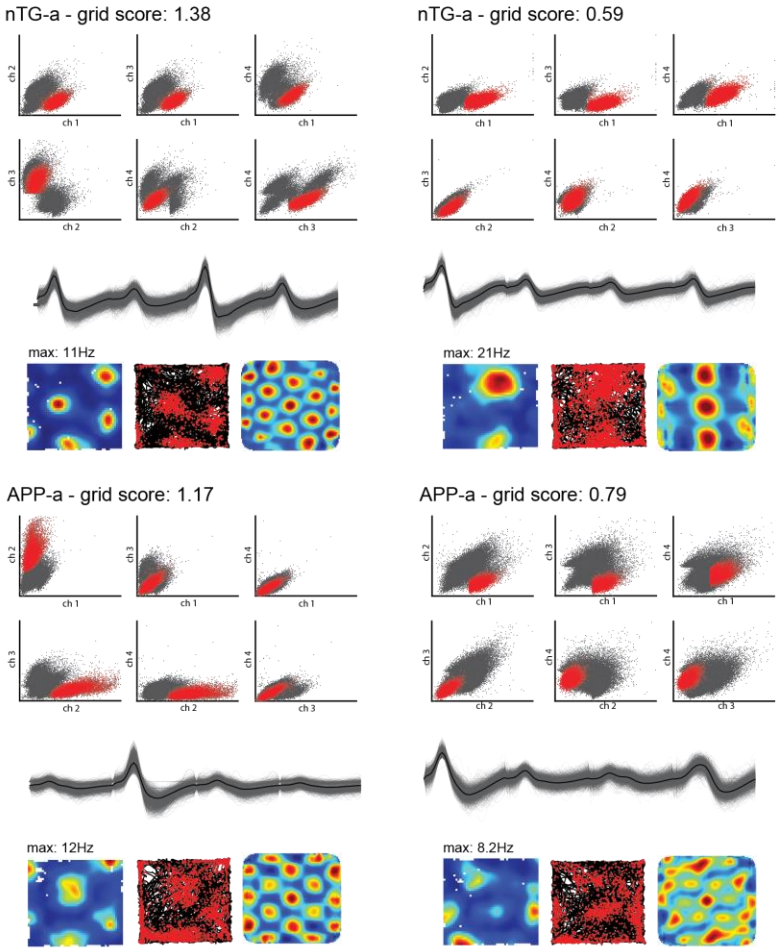

Supplementary Figure 4. Example of well-isolated waveforms of four grid cells recorded in nTG-a and APP-a mice. Cells with a high and low grid score were selected in each group for comparison. Each panel consists of the cell's grid score, the unit location in the six possible conformations of cluster space sorted by waveform amplitude, individual waveforms recorded across the four recording channels (grey) and the average waveform (black), the cell's rate map, trajectory map and rate map autocorrelation.

Supplementary Figure 5

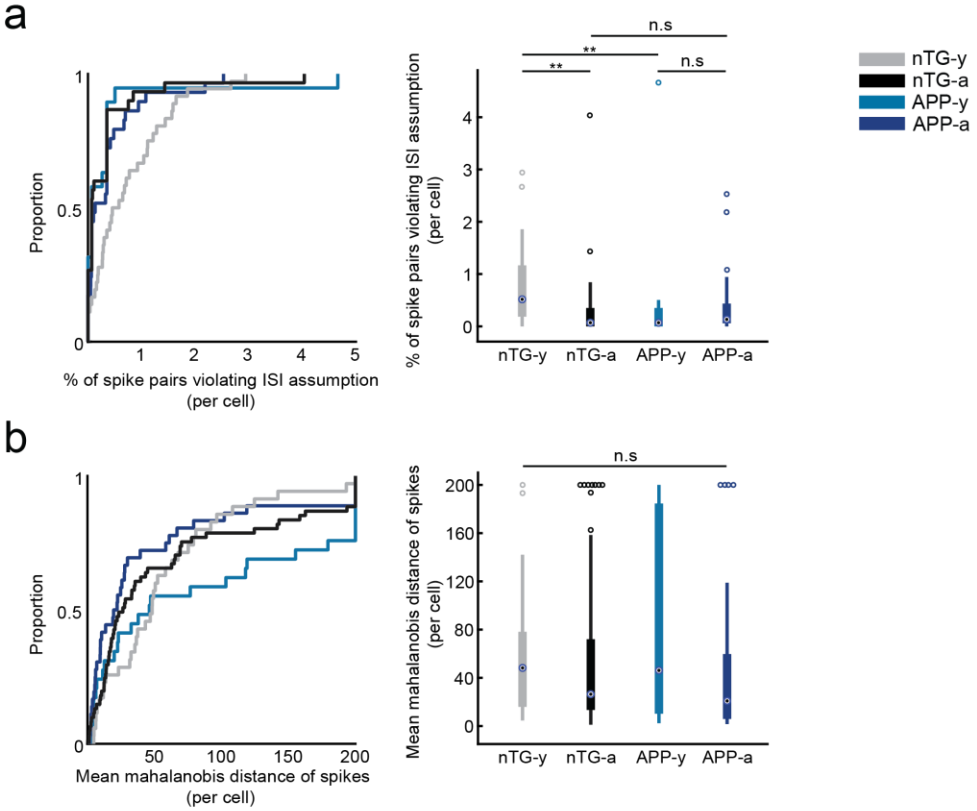

Supplementary Figure 5. Spike isolation quality of grid cells. **a,** (left) CDF plot compares the % of spike pairs with an interspike interval (ISI) less than 1 millisecond. These instances are considered non-physiological and may be due to faulty isolation or the presence of noisy spikes. (right) Box plot comparing the same thing as the CDF plot. The central dot of each bar is the median value, the edges of each bar represent the 25th and 75th percentiles, and the solid lines extend to the most extreme values not considered outliers. Separate dots are considered outliers. **b,** Same as (**a**), but comparing the mean mahalanobis distance of spikes per grid cell. ** = p<0.01, corrected for multiple comparisons.

Supplementary Figure 6

Two-way ANOVA: Grid cells

Source	Sum Square	*df*	MS	*F*	*p*
Age	2.01	1	2.01	28.26	= 0.0000002
Genotype	0.37	1	0.37	5.15	= 0.024
Interaction	0.86	1	0.86	11.99	= 0.00062
Error	19.96	280	0.07		
Total	22.65	283			

Two-way ANOVA: Head-direction cells

Source	Sum Square	*df*	MS	*F*	*p*
Age	0.19	1	0.19	3.71	= 0.054
Genotype	0.17	1	0.17	3.25	= 0.072
Interaction	0.01	1	0.01	0.2	= 0.65
Error	67.45	1311	0.05		
Total	67.77	1314			

Two-way ANOVA: Non-grid spatial cells

Source	Sum Square	*df*	MS	*F*	*p*
Age	9.41 x 10^5	1	9.41 x 10^5	0.48	= 0.49
Genotype	9.34 x 10^5	1	9.34 x 10^5	0.47	= 0.49
Interaction	7.35 x 10^5	1	7.35 x 10^5	0.37	= 0.54
Error	7.60 x 10^8	386	1.97 x 10^6		
Total	7.62 x 10^5	389			

Supplementary Figure 6. Two-way unbalanced ANOVAs comparing the effects of age, genotype, and interaction on spatial tuning scores for grid cells (grid score), head-direction cells (mean resultant length) and non-grid spatial cells (field size cm^2).

df= degrees of freedom, MS = mean square.

Supplementary Figure 7

a

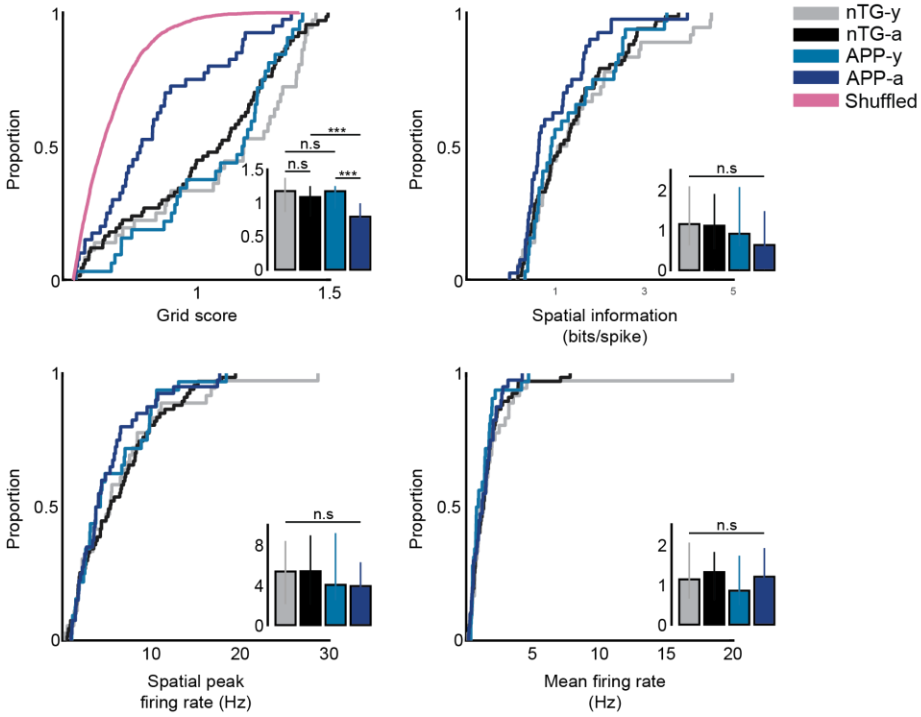

b

Two-way ANOVA: Grid cells

Source	Sum Square	*df*	MS	*F*	*p*
Age	0.90	1	0.90	12.81	= 0.00045
Genotype	0.44	1	0.44	6.31	= 0.013
Interaction	0.28	1	0.28	4.04	= 0.046
Error	12.06	171	0.07		
Total	13.62	174			

Supplementary Figure 7. Grid cell spatial tuning remains impaired in adult APP mice when duplicate cell counts are removed. **a,** CDF plots compare grid score, spatial information, spatial peak firing rate, and mean firing rate of all grid cells between experimental groups. Inset bar graphs display the median and 3rd interquartile range (solid error bars). Y-axes of all inset bar graphs indicate the value of the metric being compared by the corresponding CDF plot. ** = p<0.01, *** = p<0.001, corrected for multiple comparisons. (Grid score: nTG-y vs. nTG-a: p = 0.19, nTG-y vs. APP-y: p = 0.44, APP-y vs. APP-a: p = 0.00041, nTG-a vs. APP-a: p = 0.0031; Spatial information: nTG-y vs. nTG-a: p = 0.65, nTG-y vs. APP-y: p = 0.61, APP-y vs. APP-a: p = 0.14, nTG-a vs. APP-a: p = 0.14; Spatial peak firing rate: nTG-y vs. nTG-a: p = 0.89, nTG-y vs. APP-y: p = 0.64, APP-y vs. APP-a: p = 0.73, nTG-a vs. APP-a: p = 0.22; Mean firing rate: nTG-y vs. nTG-a: p = 0.67, nTG-y vs. APP-y: p = 0.23, APP-y vs. APP-a: p = 0.45, nTG-a vs. APP-a: p = 0.80). **b,** Two-way unbalanced ANOVAs comparing the effects of age, genotype, and interaction on grid scores for grid cells. df= degrees of freedom, MS = mean square.

Supplementary Figure 8

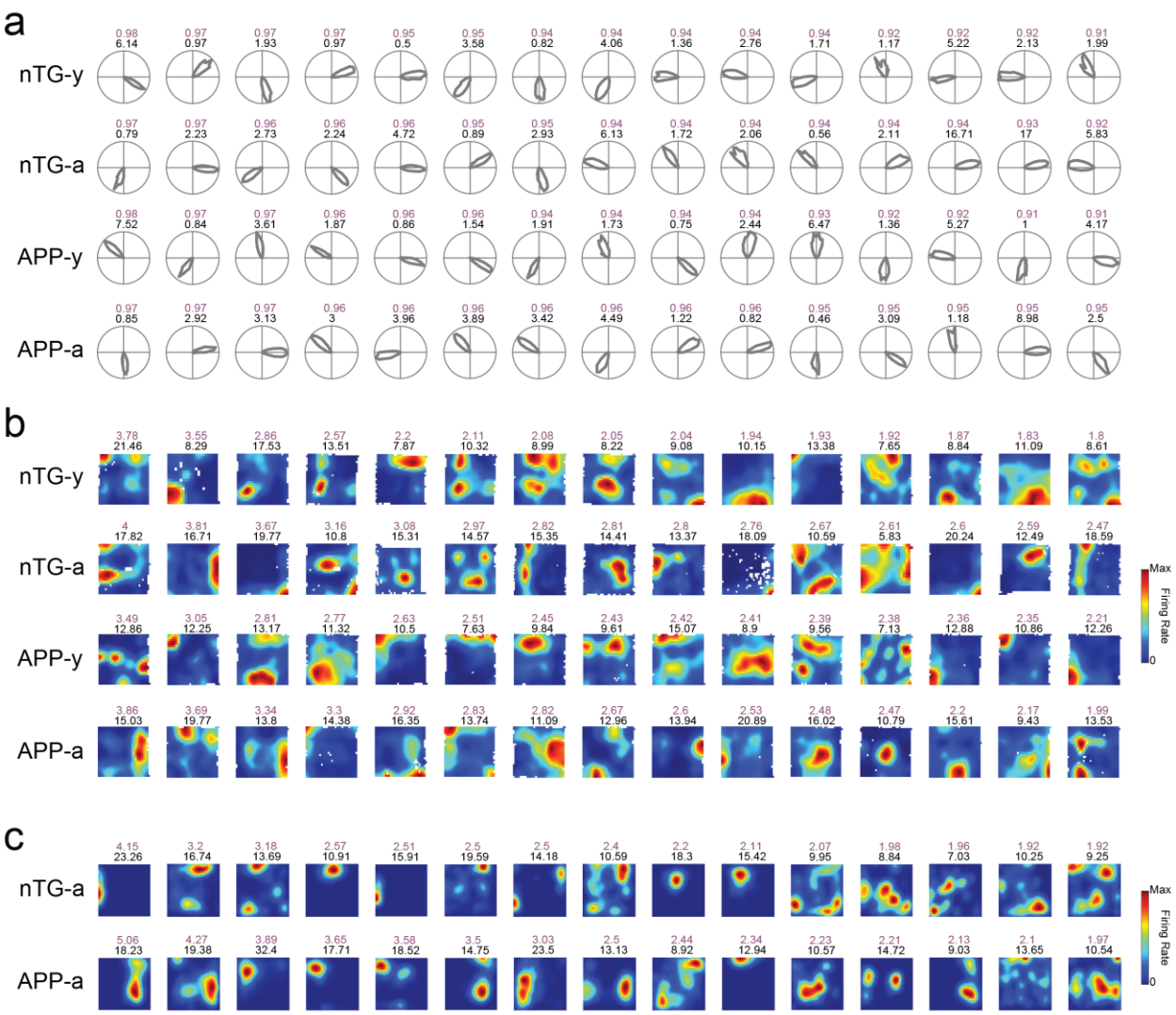

Supplementary Figure 8. Top 15 quality cells across groups. **a**, Polar rate maps for head direction cells from each experimental group. Each row includes 15 head direction cells with the highest mean resultant scores sorted in descending order. The mean resultant length (light purple) and peak firing rate (Hz) (black) of each cell are indicated on top of their respective rate maps. **b**, Same as (**a**) but for non-grid spatially-tuned cells. Cells are sorted by the highest spatial information scores in descending order. The spatial information (light purple) and peak firing rate (Hz) (black) of each cell are indicated on top of their respective rate maps. **c**, Same as (**a**) but for place cells. Cells are sorted by the highest spatial information scores in descending order. The spatial information (light purple) and peak firing rate (Hz) (black) of each cell are indicated on top of their respective rate maps.

Non-transgenic young mice (nTG-y); non-transgenic adult mice (nTG-a); APP young mice (APP-y); APP adult mice (APP-a).

Supplementary Figure 9

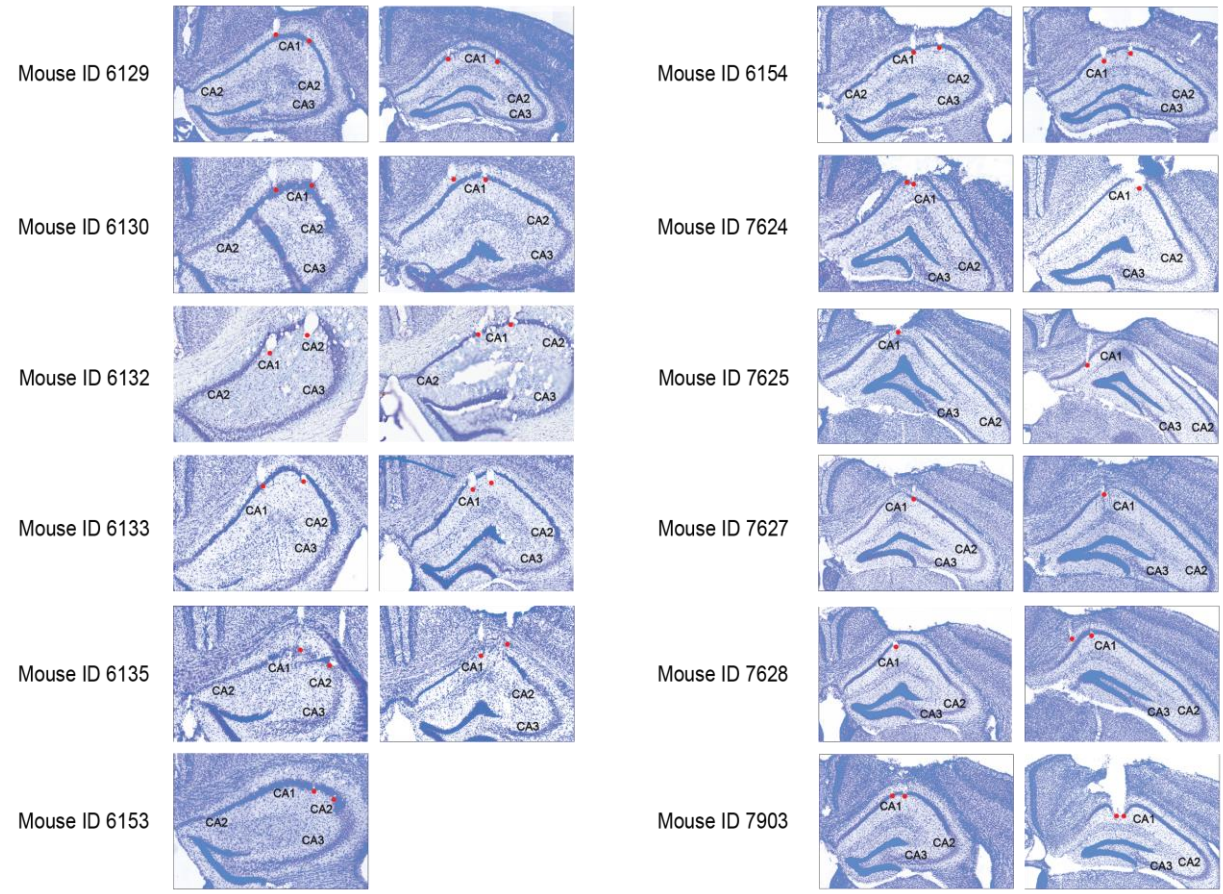

Supplementary Figure 9. Tetrode track histology for CA1 recordings. Track tips in each animal are shown in red dots.

Supplementary Figure 10

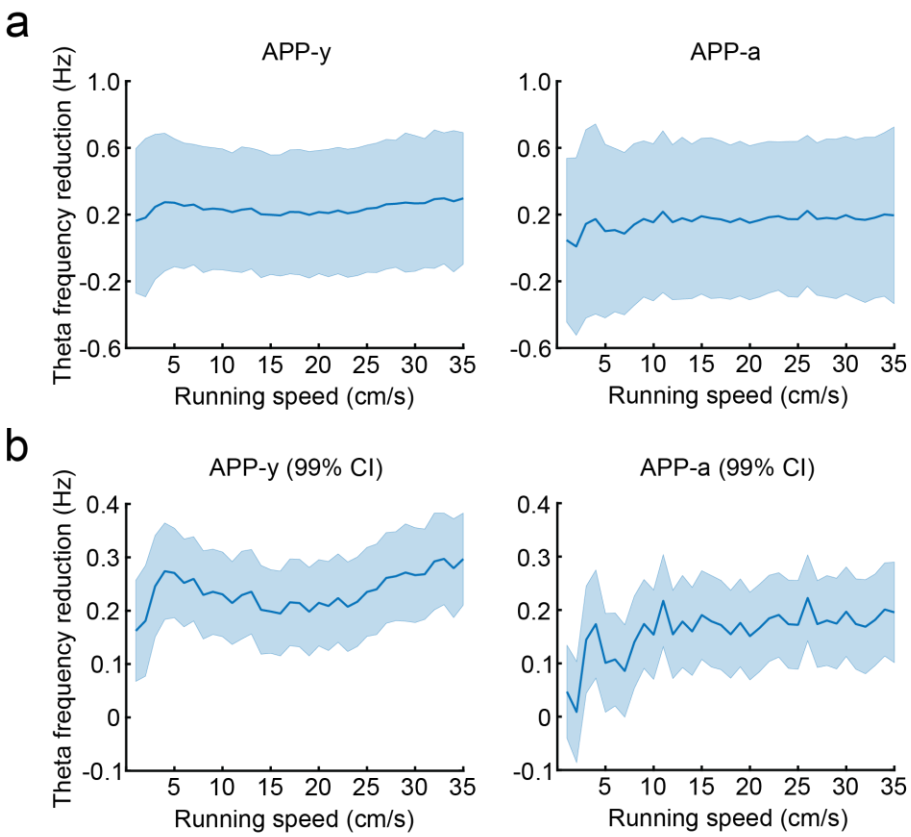

Supplementary Figure 10. The magnitude of theta frequency reduction in APP mice is roughly equal across all running speeds. **a,** Reduction of theta frequency in APP-y (left) and APP-a (right) mice across running speeds (APP mice theta frequencies were subtracted from age-matched non-transgenic counterparts). Solid blue lines indicate the mean and light blue contours indicate standard deviation. **b,** Same as (a) but values represent the 99% confidence interval.

Supplementary Figure 11

a

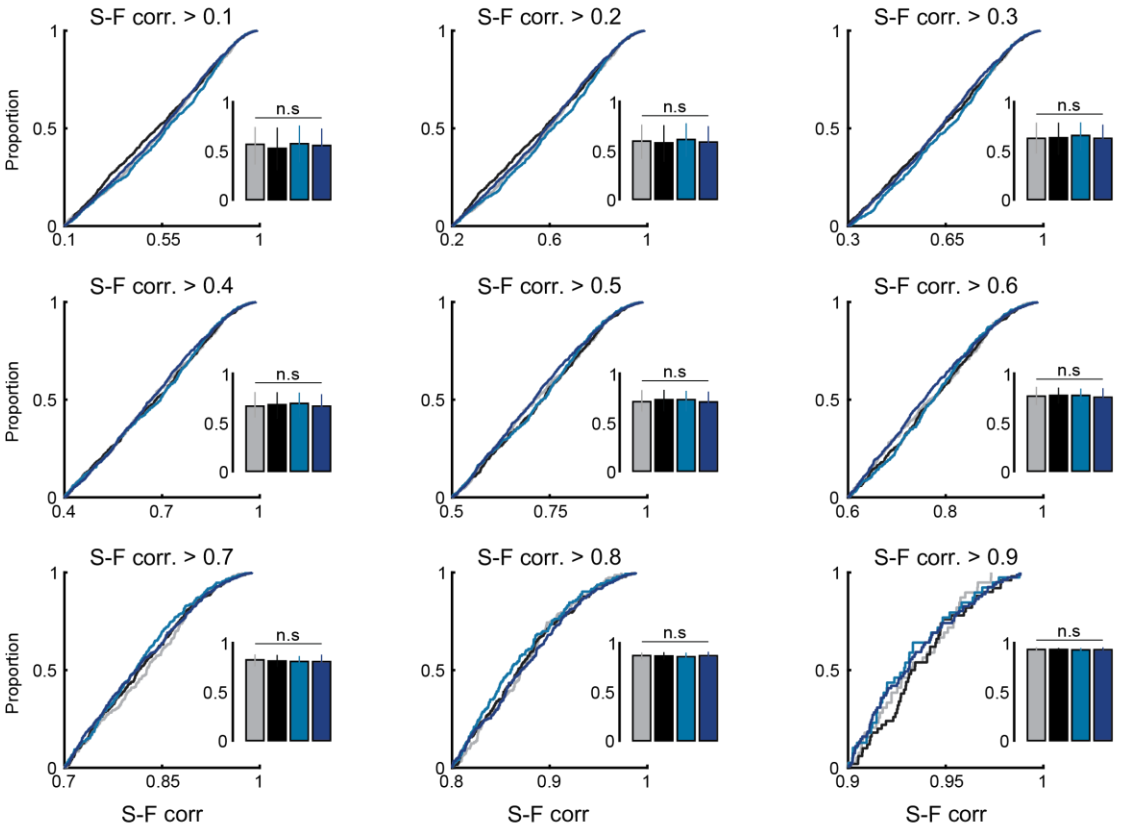

b

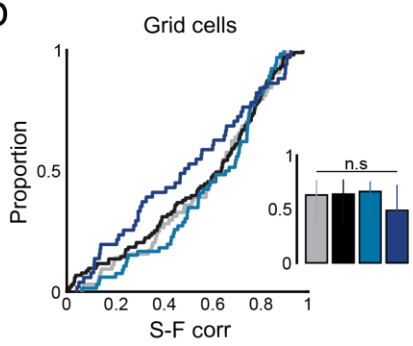

c

Two-way ANOVA: S-F corr. for grid cells

Source	Sum Square	*df*	MS	*F*	*p*
Age	0.26	1	0.26	3.9	= 0.049
Genotype	0.034	1	0.034	0.51	= 0.48
Interaction	0.12	1	0.12	1.88	= 0.17
Error	18.45	280	0.066		
Total	18.79	283			

Supplementary Figure 11. Intact speed coding in APP mice. **a,** CDF plots compare the running speed vs. firing rate correlation (S-F corr.) of putative speed cells between groups. Putative speed cells were selected based on an arbitrary S-F corr. threshold ranging from 0.1 to 0.9. Inset bar graph displays the median S-F corr. and 3rd interquartile range (solid error bar). Y-axes of all inset bar graphs indicate the S-F corr. **b,** Same as (**a**) but panels compare the S-F corr. for grid cells. Grid-Interneuron: nTG-y vs. nTG-a: p = 0.78, nTG-y vs. APP-y: p = 0.67, APP-y vs. APP-a: p = 0.059, nTG-a vs. APP-a: p = 0.20). **c,** Two-way unbalanced ANOVAs comparing the effects of age, genotype, and interaction on the S-F corr. for grid cells across groups. df= degrees of freedom, MS = mean square.

Supplementary Figure 12

Two-way ANOVA: Mean 2D displacement

Source	Sum Square	*df*	MS	*F*	*p*
Genotype	33.79	1	33.79	8.43	= 0.0038
Cell type	38.57	2	19.29	4.81	= 0.0084
Interaction	34.83	2	17.41	4.34	= 0.013
Error	3296.64	822	4.01		
Total	3410.74	827			

Pairwise comparisons: Tukey's test

		95% C.I. for true mean diff.		
Comparisons	Mean diff.	LL	UL	*p*
nTG-a grid - APP-a grid	**-1.23**	**-2.23**	**-0.23**	**0.0064**
nTG-a grid - nTG-a nongrid	-0.69	-1.56	0.17	0.2
nTG-a grid - APP-a nongrid	-0.79	-1.58	0.00	0.049
nTG-a grid - nTG-a place	-1.08	-1.77	-0.39	0.00012
nTG-a grid - APP-a place	-1.18	-1.87	-0.49	1.60E-05
APP-a grid - nTG-a nongrid	0.54	-0.50	1.57	0.68
APP-a grid - APP-a nongrid	0.44	-0.54	1.41	0.8
APP-a grid - nTG-a place	0.15	-0.75	1.04	1
APP-a grid - APP-a place	0.05	-0.84	0.94	1
nTG-a nongrid - APP-a nongrid	**-0.10**	**-0.93**	**0.73**	**1**
nTG-a nongrid - nTG-a place	-0.39	-1.13	0.35	0.66
nTG-a nongrid - APP-a place	-0.49	-1.22	0.25	0.41
APP-a nongrid - nTG-a place	-0.29	-0.94	0.36	0.8
APP-a nongrid - APP-a place	-0.39	-1.03	0.26	0.53
nTG-a place - APP-a place	**-0.10**	**-0.61**	**0.42**	**0.99**

Supplementary Figure 12. Two-way unbalanced ANOVAs comparing the effects of genotype, cell type, and interaction on the mean 2D displacement scores for grid cells, non-grid spatially-tuned cells and place cells. Grid cells, non-grid spatially-tuned cells and place cells were included in the "Cell type" factor. Multiple pairwise comparisons with Tukey's test at a corrected alpha value of 0.05 are shown at the bottom. The 3 comparisons of interest (nTG-a grid - APP-a grid; nTG-a nongrid - APP-a nongrid; nTG-a place - APP-a place) are bolded.

df= degrees of freedom, MS = mean square.

Supplementary Figure 13. Page 1

a

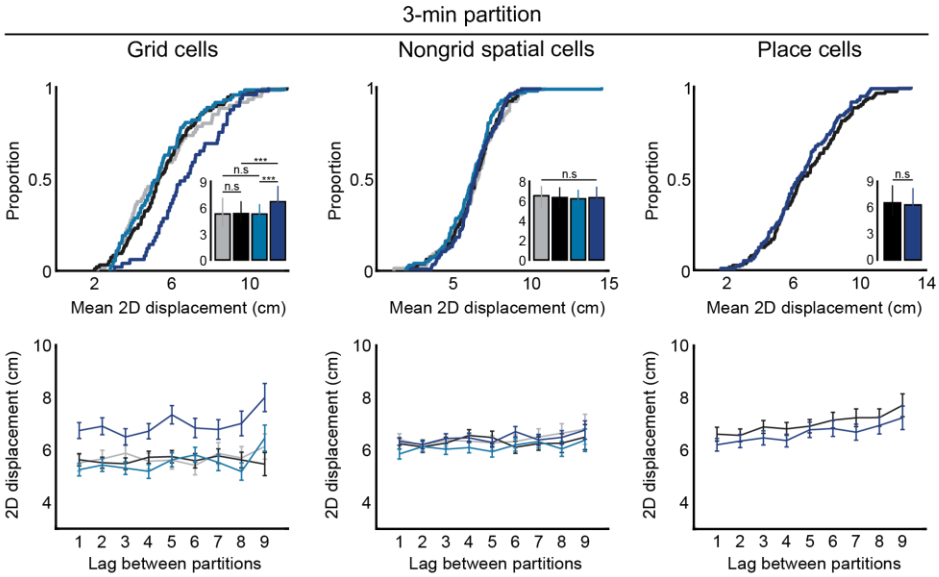

b

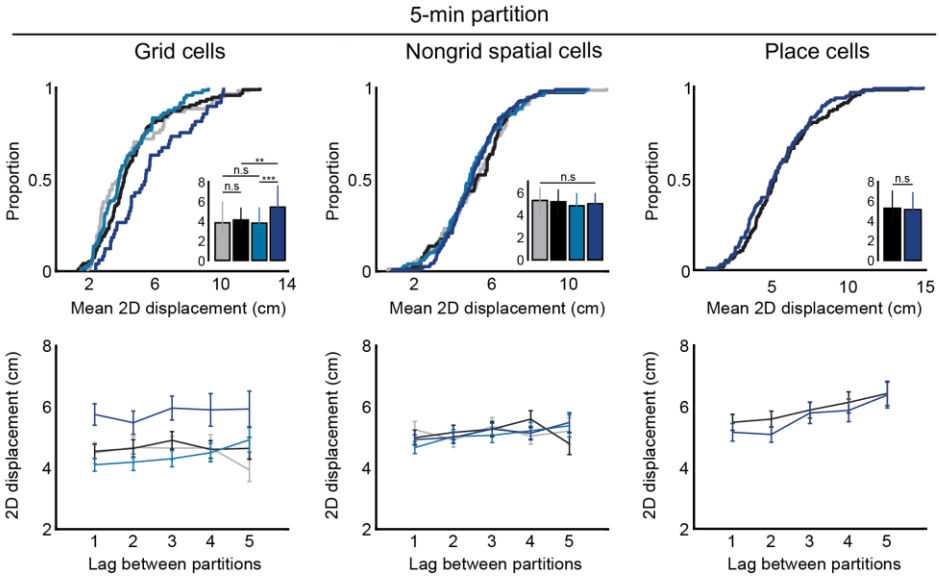

Supplementary Figure 13. Page 2

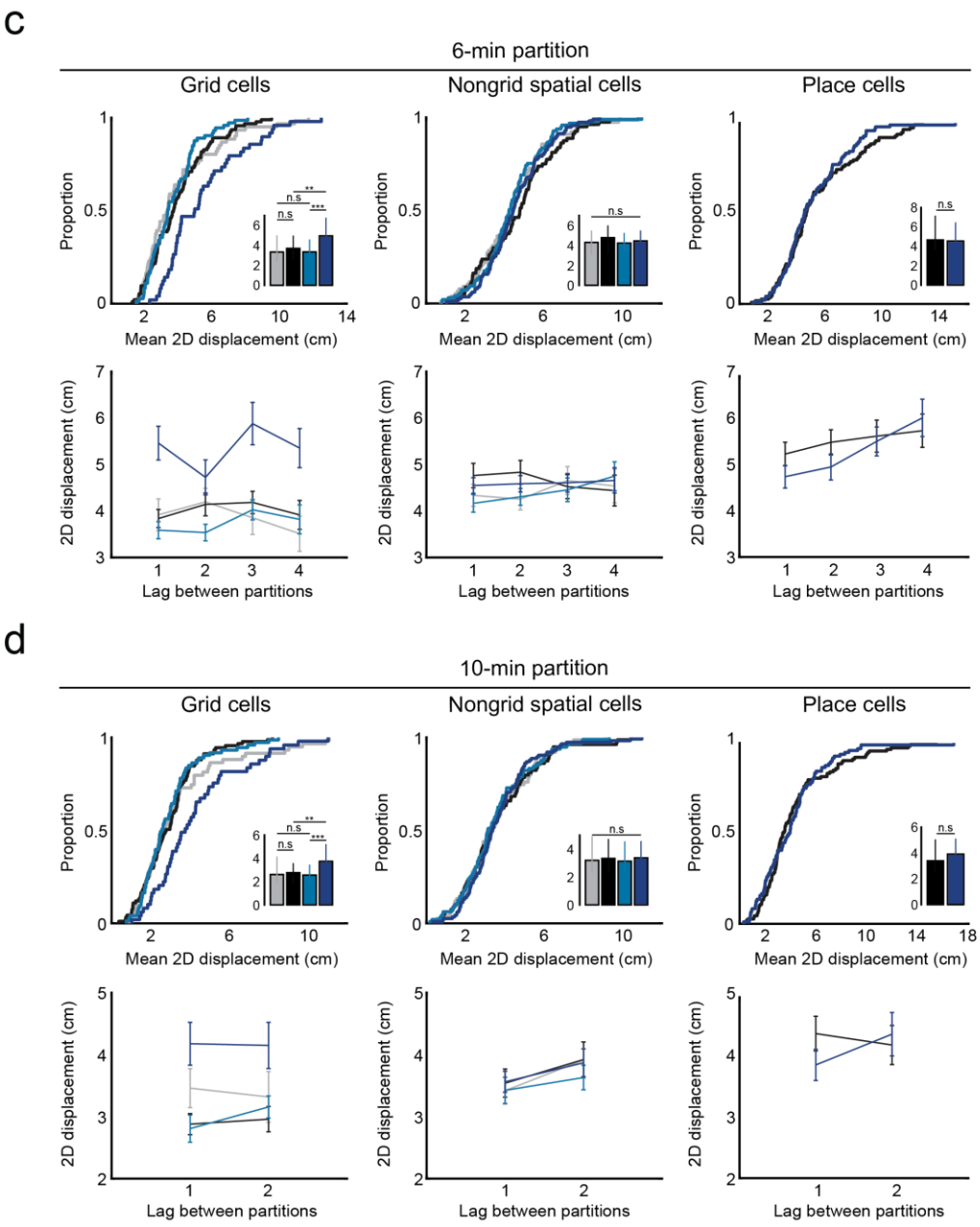

Supplementary Figure 13. Reduced grid cell spatial stability in adult APP mice persists across different partition lengths. **a,** 3-minute partition analyses. (top-row) CDF plots compare the mean two dimensional displacement of grid cells, non-grid spatially-tuned cells and place cells between groups. Inset bar graph displays the median displacement and 3rd interquartile range (solid error bar). Y-axes of all inset bar graphs indicate the mean two dimensional displacement. (Grid cells: nTG-y vs. nTG-a: p = 0.76, nTG-y vs. APP-y: p = 0.76, APP-y vs. APP-a: p = 0.00091, nTG-a vs. APP-a: p = 0.00034; Nongrid spatial cells: nTG-y vs. nTG-a: p = 0.74, nTG-y vs. APP-y: p = 0.24, APP-y vs. APP-a: p = 0.19, nTG-a vs. APP-a: p = 0.87; Place cells: nTG-a vs. APP-a: p = 0.37). (bottom-row) Two dimensional displacement of grid cells, non-grid spatially-tuned cells and place cells as a function of lags between partitions. Dots indicate mean values and error bars indicate standard error of mean. **b, c, d,** Same as (**a**) but panels compare 5-minute, 6-minute, and 10-minute partitions respectively. (*5 min partitions:* Grid cells: nTG-y vs. nTG-a: p = 0.35, nTG-y vs. APP-y: p = 0.98, APP-y vs. APP-a: p = 0.0019, nTG-a vs. APP-a: p = 0.01; Nongrid spatial cells: nTG-y vs. nTG-a: p = 0.92, nTG-y vs. APP-y: p = 0.35, APP-y vs. APP-a: p = 0.65, nTG-a vs. APP-a: p = 0.58; Place cells: nTG-a vs. APP-a: p = 0.67). (*6 min partitions:* Grid cells: nTG-y vs. nTG-a: p = 0.39, nTG-y vs. APP-y: p = 1, APP-y vs. APP-a: p = 0.00006, nTG-a vs. APP-a: p = 0.0025; Nongrid spatial cells: nTG-y vs. nTG-a: p = 0.31, nTG-y vs. APP-y: p = 0.96, APP-y vs. APP-a: p = 0.41, nTG-a vs. APP-a: p = 0.67; Place cells: nTG-a vs. APP-a: p = 0.47). (*10 min partitions:* Grid cells: nTG-y vs. nTG-a: p = 0.93, nTG-y vs. APP-y: p = 0.53, APP-y vs. APP-a: p = 0.00084, nTG-a vs. APP-a: p = 0.0026; Nongrid spatial cells: nTG-y vs. nTG-a: p = 0.92, nTG-y vs. APP-y: p = 0.65, APP-y vs. APP-a: p = 0.35, nTG-a vs. APP-a: p = 0.79; Place cells: nTG-a vs. APP-a: p = 0.61). ** = p<0.01, *** = p<0.001, corrected for multiple comparisons.

Supplementary Figure 14

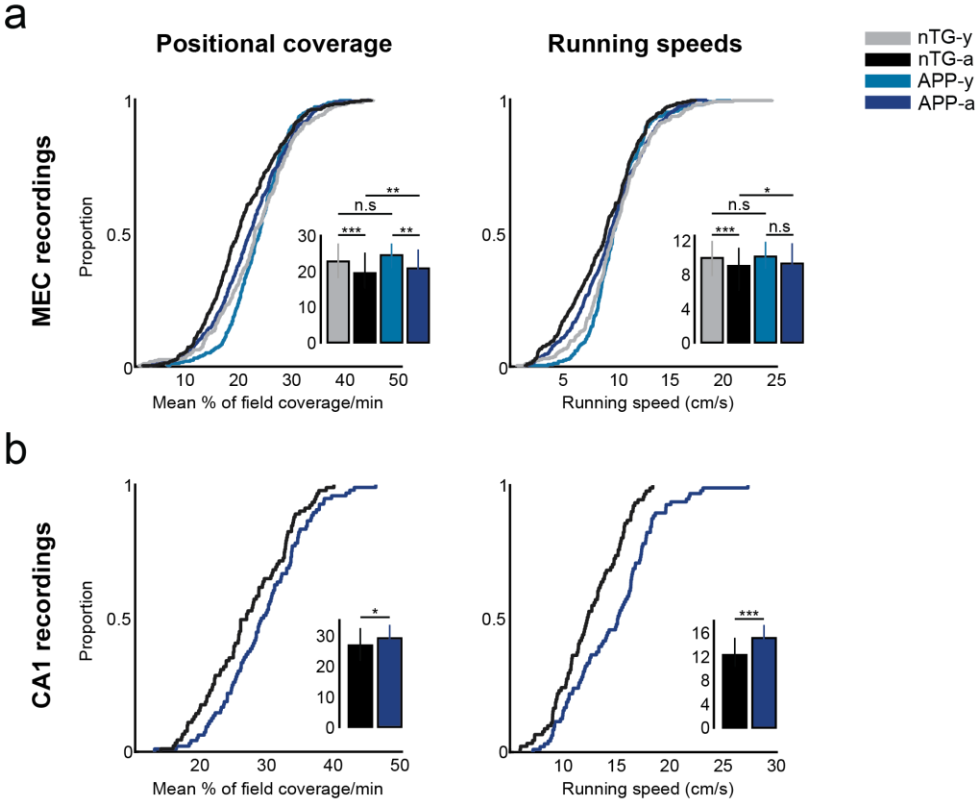

Supplementary Figure 14. Positional coverage and running speeds across groups for MEC and CA1 recordings. **a,** CDF plots compare the mean % of the environment covered per minute and average running speed between experimental groups for MEC recordings. Inset bar graphs display the median and 3rd interquartile range (solid error bars). Y-axes of all inset bar graphs indicate the value of the metric being compared by the corresponding CDF plot. (Mean % of field coverage/min: nTG-y vs. nTG-a: p = 0.000033, nTG-y vs. APP-y: p = 0.51, APP-y vs. APP-a: p = 0.0053, nTG-a vs. APP-a: p = 0.0041; Running speed: nTG-y vs. nTG-a: p = 0.00091, nTG-y vs. APP-y: p = 0.91, APP-y vs. APP-a: p = 0.099, nTG-a vs. APP-a: p = 0.047). **b,** Same as (**a**), but for CA1 recordings. (Mean % of field coverage/min: nTG-a vs. APP-a: p = 0.017; Running speed: nTG-a vs. APP-a: p = 0.00014). * = p<0.05, ** = p<0.01, *** = p<0.001, corrected for multiple comparisons.

Supplementary Figure 15

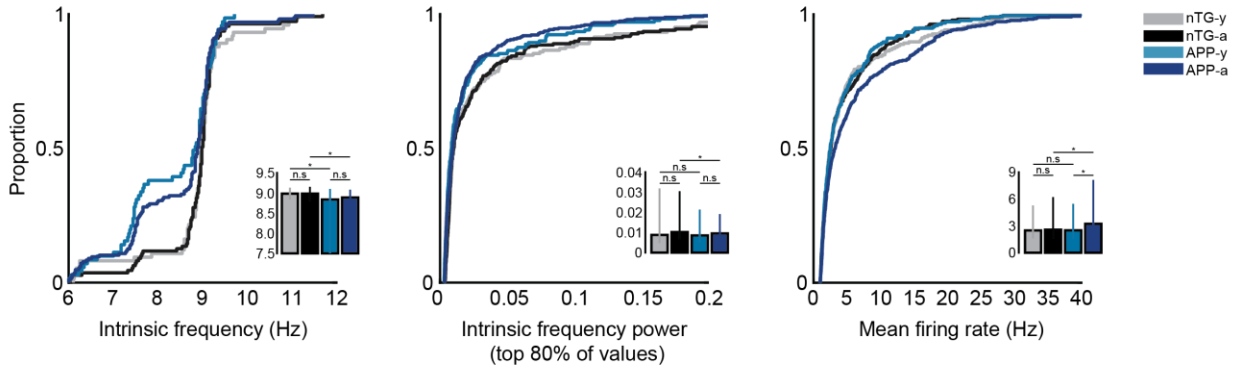

Supplementary Figure 15. Interneuron firing properties. Cumulative distribution functions (CDFs) compare the intrinsic frequency, intrinsic frequency power (for the top 80% of values), and mean firing rates of interneurons between experimental groups. Inset bar graphs display the median and 3rd interquartile range (solid error bars). Y-axes of inset bar graphs indicate the value of the metric being compared by the corresponding CDF plot. (Intrinsic frequency: nTG-y vs. nTG-a: p = 0.99, nTG-y vs. APP-y: p = 0.038, APP-y vs. APP-a: p = 0.49, nTG-a vs. APP-a: p = 0.023; Intrinsic frequency power (top 80% of values): nTG-y vs. nTG-a: p = 0.056, nTG-y vs. APP-y: p = 0.58, APP-y vs. APP-a: p = 0.38, nTG-a vs. APP-a: p = 0.034; Mean firing rate: nTG-y vs. nTG-a: p = 0.95, nTG-y vs. APP-y: p = 0.82, APP-y vs. APP-a: p = 0.034, nTG-a vs. APP-a: p = 0.028). * = p<0.05, corrected for multiple comparisons.

Supplementary Figure 16

Two-way ANOVA: Intrinsic frequency (Hz)

Source	Sum Square	*df*	MS	*F*	*p*
Age	0.58	1	0.58	0.60	= 0.44
Genotype	20.42	1	20.42	21.23	= 0.0000054
Interaction	0.61	1	0.61	0.63	= 0.43
Error	403.04	419	0.96		
Total	423.90	422			

Two-way ANOVA: Intrinsic frequency power (top 80% of values)

Source	Sum Square	*df*	MS	*F*	*p*
Age	9 x 10^-5	1	9 x 10^-5	0.03	= 0.85
Genotype	3.74 x 10^-2	1	3.74 x 10^-2	14.72	= 0.0001
Interaction	5.80 x 10^-4	1	5.80 x 10^-4	0.23	= 0.63
Error	2.28	897	2.54 x 10^-3		
Total	2.33	900			

Two-way ANOVA: Mean firing rate (Hz)

Source	Sum Square	*df*	MS	*F*	*p*
Age	147.70	1	147.70	3.06	= 0.081
Genotype	63.60	1	63.60	1.32	= 0.25
Interaction	326.10	1	326.10	6.75	= 0.0095
Error	5.42 x 10^4	1123	48.34		
Total	5.50 x 10^4	1126			

Supplementary Figure 16. Two-way unbalanced ANOVAs comparing the effects of age, genotype, and interaction on the intrinsic frequency, intrinsic frequency power (for the top 80% of values), and mean firing rates of interneurons between experimental groups.

df= degrees of freedom, MS = mean square.

Supplementary Figure 17

Two-way ANOVA: Grid cell-interneuron synchrony

Source	Sum Square	*df*	MS	*F*	*p*
Age	2.38	1	2.38	0.27	= 0.60
Genotype	173.58	1	173.58	19.8	= 0.000013
Interaction	25.16	1	25.17	2.87	= 0.09
Error	2270.69	259	8.77		
Total	2520.39	262			

Two-way ANOVA: Grid cell-head direction cell synchrony

Source	Sum Square	*df*	MS	*F*	*p*
Age	37.53	1	37.53	7.07	= 0.0083
Genotype	34.11	1	34.11	6.43	= 0.0119
Interaction	16.08	1	16.08	3.03	= 0.08
Error	1289.16	243	5.31		
Total	1356.97	246			

Supplementary Figure 17. Two-way unbalanced ANOVAs comparing the effects of age, genotype, and interaction on the mean co-activity within a 25 ms time window for grid cell-interneuron pairs, and grid cell-head direction cell pairs.

df= degrees of freedom, MS = mean square.

Supplementary Figure 18

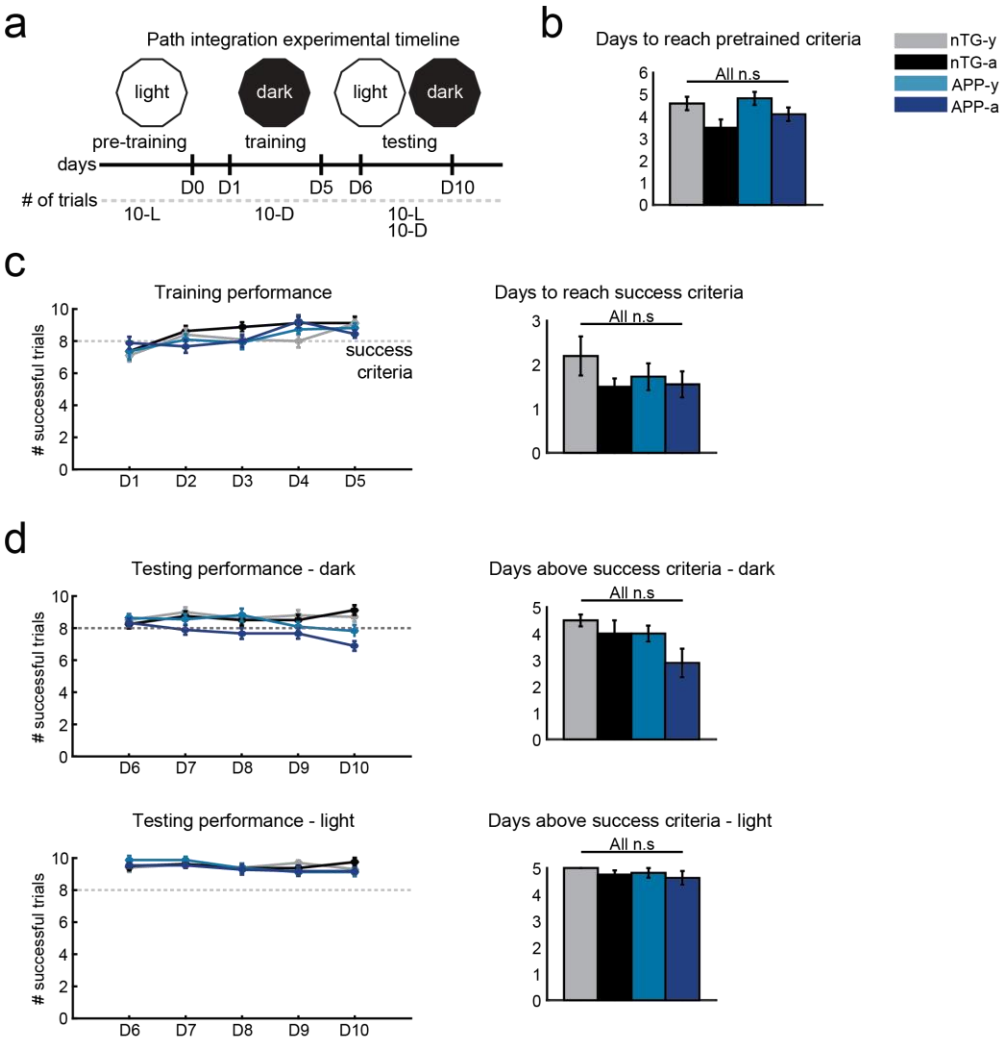

Supplementary Figure 18. Experimental timeline for the path integration task and mouse performance across days. **a**, Experimental timeline for the food-foraging task. Days are indicated as D0, D1, etc. The number of trials that each mouse performed are indicated as 10-L (i.e. 10 light trials) and 10-D (i.e. 10 dark trials). **b**, The number of days that it took mice in each group to achieve the success criteria in the pre-training phase (8/10 successful trials). (nTG-y vs. nTG-a: p = 0.079, nTG-y vs. APP-y: p = 0.65, APP-y vs. APP-a: p = 0.24, nTG-a vs. APP-a: p = 0.28). **c**, (Left) The number of successful trials achieved by mice across 5 days of training. (Right) The number of days within this training period that mice took to reach the success criteria. (nTG-y vs. nTG-a: p = 0.42, nTG-y vs. APP-y: p = 0.45, APP-y vs. APP-a: p = 0.70, nTG-a vs. APP-a: p = 0.84). **d**, (Top-Left) Same as (**c**) but across 5 days of testing in dark conditions. (Top-Right) The number of days within this testing period that mice performed at or above the success criteria. (nTG-y vs. nTG-a: p = 0.60, nTG-y vs. APP-y: p = 0.24, APP-y vs. APP-a: p = 0.11, nTG-a vs. APP-a: p = 0.11). (Bottom-Left) Same as (**c**) but across 5 days of testing in light conditions. (Bottom-Right) The number of days within this testing period that mice performed at or above the success criteria. (nTG-y vs. nTG-a: p = 0.37, nTG-y vs. APP-y: p = 0.39, APP-y vs. APP-a: p = 0.75, nTG-a vs. APP-a: p = 1). Bars indicate mean values and error bars indicate standard error of mean.

Supplementary Figure 19

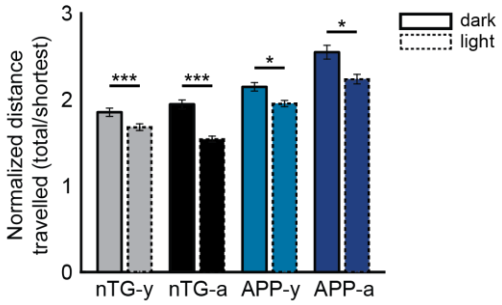

Supplementary Figure 19. Overall navigation ability improves in light trials for all mice. Bar graph compares the normalized distance travelled in dark (solid lines) versus light (dashed lines) trials. Bars indicate mean values and error bars indicate standard error of mean. (nTG-y: p = 2.1e-8; nTG-a: p = 5.7e-21; APP-y: p = 0.017; APP-a: p = 0.017). * = p<0.05, *** = p<0.001, corrected for multiple comparisons.

Supplementary Figure 20

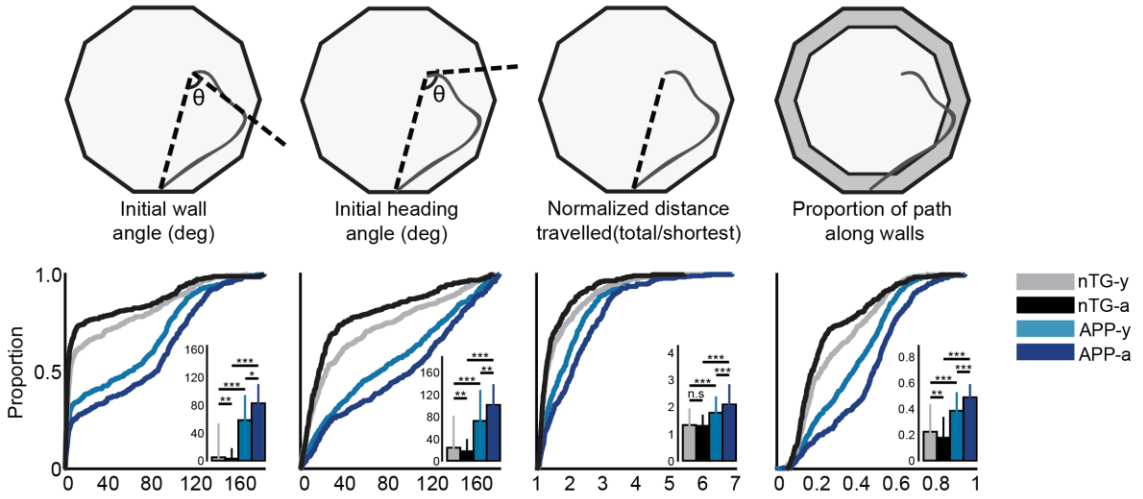

Supplementary Figure 20. APP mice have impaired path integration ability in light conditions. CDF plots compare the initial wall angle, the initial heading angle, the normalized distance travelled and the proportion of the return path spent along the periphery between groups. Inset bar graphs display the median and 3rd interquartile range (solid error bars). Y-axes of all inset bar graphs indicate the value of the metric being compared by the corresponding CDF plot. The calculation of each metric is shown in schematics above their respective plots. (Initial wall angle: nTG-y vs. nTG-a: p = 0.0075, nTG-y vs. APP-y: p = 1.1e-18, APP-y vs. APP-a: p = 0.013, nTG-a vs. APP-a: p = 1.5e-32; Initial heading angle: nTG-y vs. nTG-a: p = 0.0029, nTG-y vs. APP-y: p = 3.4e-17, APP-y vs. APP-a: p = 0.0044, nTG-a vs. APP-a: p = 1.2e-33; Normalized distance travelled: nTG-y vs. nTG-a: p = 0.053, nTG-y vs. APP-y: p = 7.7e-12, APP-y vs. APP-a: p = 6.3e-5, nTG-a vs. APP-a: p = 1.2e-26; Proportion of path along walls: nTG-y vs. nTG-a: p = 0.0015, nTG-y vs. APP-y: p = 8.2e-13, APP-y vs. APP-a: p = 9.5e-9, nTG-a vs. APP-a: p = 9.3e-35). * = p<0.05, ** = p<0.01, *** = p<0.001, corrected for multiple comparisons.

Supplementary Figure 21

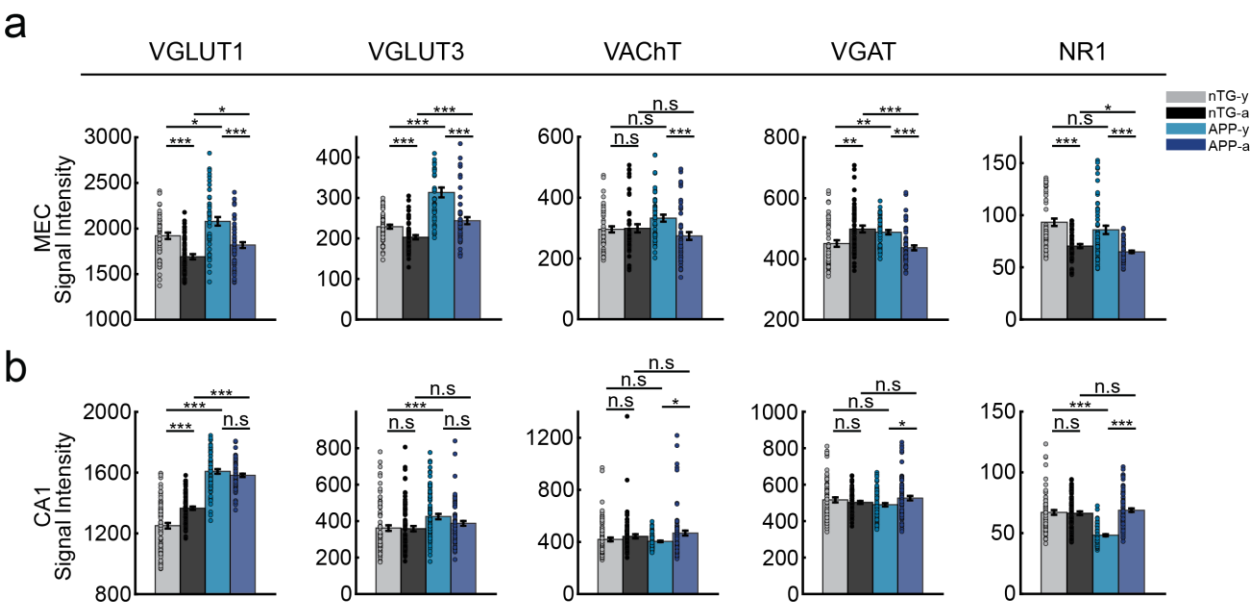

Supplementary Figure 21. Immunoautoradiographic labelling of synaptic markers in the MEC and CA1. **a,** Bar graphs compare signal intensity of VGLUT1, VGLUT3, VAChT, VGAT and NR1 synaptic markers in the MEC. Bars indicate mean and error bars indicate standard error of mean. Individual data points are scattered. (VGLUT1: nTG-y vs. nTG-a: p = 1.3e-5, nTG-y vs. APP-y: p = 0.014, APP-y vs. APP-a: p = 1.1e-4, nTG-a vs. APP-a: p = 0.014; VGLUT3: nTG-y vs. nTG-a: p = 1.9e-4, nTG-y vs. APP-y: p = 1.5e-8, APP-y vs. APP-a: p = 2.6e-6, nTG-a vs. APP-a: p = 2.3e-4; VAChT: nTG-y vs. nTG-a: p = 0.87, nTG-y vs. APP-y: p = 0.053, APP-y vs. APP-a: p = 4.5e-4, nTG-a vs. APP-a: p = 0.051; VGAT: nTG-y vs. nTG-a: p = 0.0037, nTG-y vs. APP-y: p = 0.0027, APP-y vs. APP-a: p = 7.4e-6, nTG-a vs. APP-a: p = 2.1e-5; NR1: nTG-y vs. nTG-a: p = 1.6e-5, nTG-y vs. APP-y: p = 0.063, APP-y vs. APP-a: p = 2.7e-5, nTG-a vs. APP-a: p = 0.023). **b,** Same as (**a**), but for CA1. (VGLUT1: nTG-y vs. nTG-a: p = 4.6e-6, nTG-y vs. APP-y: p = 3.9e-21, APP-y vs. APP-a: p = 0.15, nTG-a vs. APP-a: p = 4.5e-21; VGLUT3: nTG-y vs. nTG-a: p = 0.76, nTG-y vs. APP-y: p = 5.7e-4, APP-y vs. APP-a: p = 0.066, nTG-a vs. APP-a: p = 0.10; VAChT: nTG-y vs. nTG-a: p = 0.14, nTG-y vs. APP-y: p = 0.30, APP-y vs. APP-a: p = 0.039, nTG-a vs. APP-a: p = 0.39; VGAT: nTG-y vs. nTG-a: p = 0.87, nTG-y vs. APP-y: p = 0.33, APP-y vs. APP-a: p = 0.074, nTG-a vs. APP-a: p = 0.35; NR1: nTG-y vs. nTG-a: p = 0.71, nTG-y vs. APP-y: p = 2.1e-14, APP-y vs. APP-a: p = 9.4e-19, nTG-a vs. APP-a: p = 0.41). * = p<0.05, ** = p<0.01, *** = p<0.001, corrected for multiple comparisons.

Supplementary Figure 22

a

Linear mixed effects model predicting VGLUT3 expression in the MEC

Model information

Number of observations : 198
Fixed effects coefficients : 3
Random effects coefficients : 48
Covariance parameters : 4

Model fit statistics

AIC : 2071.4
BIC : 2094.4
Log Likelihood : -1028.7
Deviance : 2057.4

Fixed effects coefficients (95% CIs):

Name	Estimate	Std. Error	tStat	DF	*p*	*95% CI* LL	*95% CI* UL
Intercept	253.03	18.12	13.96	195	= 3.6e-31	217.29	288.77
Genotype	-60.5	21.78	-2.78	195	= 0.006	-103.45	-17.55
Age	48.23	21.96	2.2	195	= 0.0292	4.93	91.55

Random effects covariance (95% CIs):

Subject(16 levels)	Estimate	*95% CI* LL	*95% CI* UL
Intercept	39.48	25.95	60.05
* Genotype	< 0.001	NaN	NaN
* Age	22.15	19.98	24.56

Error	Estimate	*95% CI* LL	*95% CI* UL
Residual	39.1	35.29	43.33

b

Linear mixed effects model predicting VGLUT1 expression in CA1

Model information

Number of observations : 308
Fixed effects coefficients : 3
Random effects coefficients : 48
Covariance parameters : 4

Model fit statistics

AIC : 3687.8
BIC : 3713
Log Likelihood : -1836.9
Deviance : 3673.8

Fixed effects coefficients (95% CIs):

Name	Estimate	Std. Error	tStat	DF	*p*	*95% CI* LL	*95% CI* UL
Intercept	1590.7	21.47	74.09	305	= 4.8e-197	1548.5	1633
Genotype	-270.68	45.09	-6	305	= 5.5e-9	-359.41	-181.9
Age	-3.91	38.68	-0.1	305	= 0.92	-80.02	72.2

Random effects covariance (95% CIs):

Subject(16 levels)	Estimate	*95% CI* LL	*95% CI* UL
Intercept	39.6	17.22	91.03
* Genotype	96.99	30.2	311.5
* Age	61.3	9.05	415.14

Error	Estimate	*95% CI* LL	*95% CI* UL
Residual	84.54	80.72	94.93

Supplementary Figure 22. We used the fitlme function in MATLAB to perform linear mixed effects analyses on the relationship between the subjects' genotype (nTG and APP), age (young and adult) and expression of VGLUT3 and VGLUT1 levels in the MEC and CA1 respectively. The fixed effects of the model comprised genotype and age (without interaction between the two). The random effects of the model comprised random intercepts by-subject, random slopes for the effects of genotype and age by-subject, and independence between the intercepts and slopes. P-values obtained in the model output were considered as the measurements for significance.

a, Table shows the model information, statistics of fit, the fixed effects coefficients, and the random effects covariance parameters. In the fixed effects panel, the 'Intercept' refers to the aged APP experimental group; its estimate is the predicted mean VGLUT3 signal intensity. The estimates for genotype and age refer to the predicted slope change from the intercept. Std. Error refers to the standard error associated with the slope. T-values and P-values for the contribution of genotype and age are bolded. **b,** Same as (**a**) but for levels of VGLUT1 in CA1.

tStat = T-value, CI = confidence interval, DF = degrees of freedom, LL = lower limit, UL = upper limit.
* = independence between intercepts and slopes.

Supplementary Figure 23

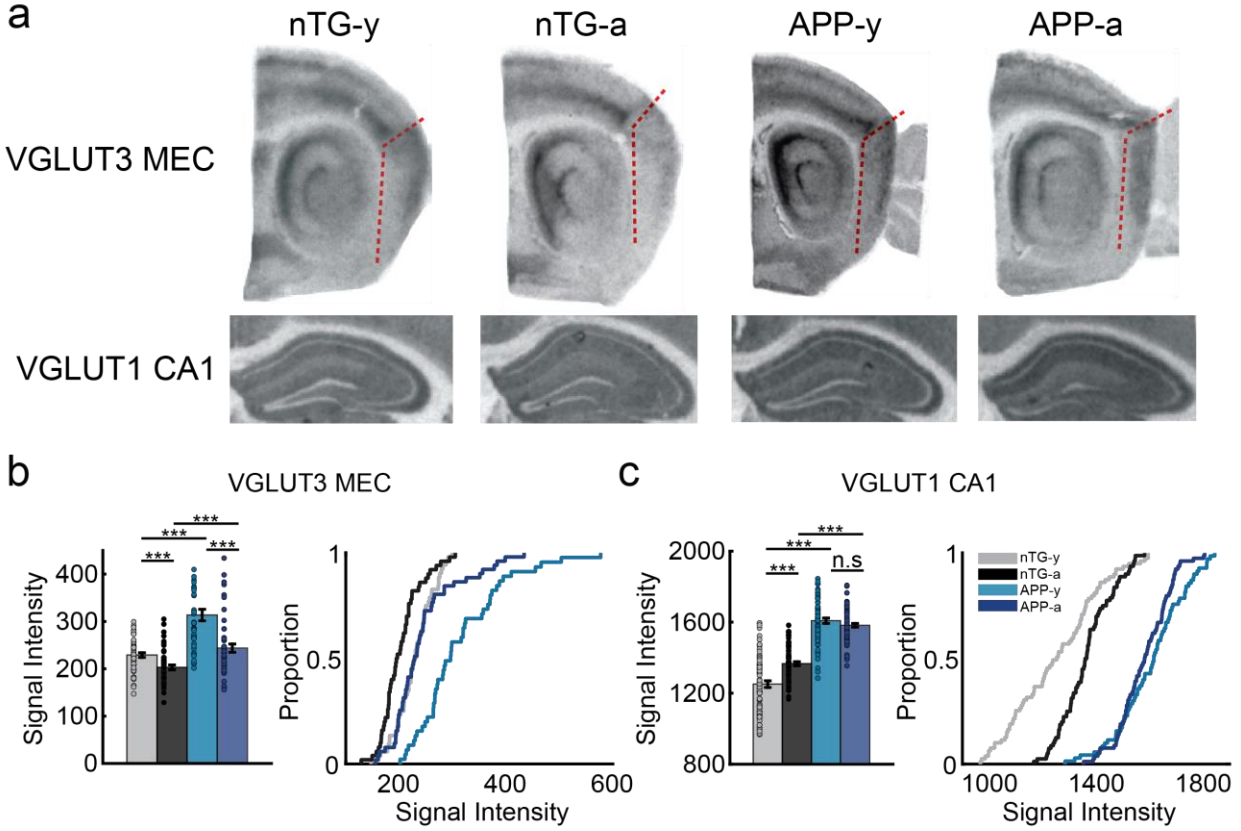

Supplementary Figure 23. Pathological expression of MEC VGLUT3 levels and CA1 VGLUT1 levels in APP mice. **a,** Single slice examples of VGLUT3 and VGLUT1 expression in MEC and CA1 respectively. Darker signals indicate higher marker expression levels. **b,** (left) Bar graph shows signal intensity of VGLUT3 levels in the MEC between experimental groups. Error bars indicate standard error of mean, and individual sample points are scattered. (right) Cumulative distribution function (CDF) compares the signal intensity between experimental groups. (nTG-y vs. nTG-a: p = 1.9e-4, nTG-y vs. APP-y: p = 1.5e-8, APP-y vs. APP-a: p = 2.6e-6, nTG-a vs. APP-a: p = 2.3e-4). **c,** Same as (**b**), but panels compare signal intensity of VGLUT1 levels in the CA1 between experimental groups. (nTG-y vs. nTG-a: p = 4.6e-6, nTG-y vs. APP-y: p = 3.9e-21, APP-y vs. APP-a: p = 0.15, nTG-a vs. APP-a: p = 4.5e-21). * = p<0.05, ** = p<0.01, *** = p<0.001, corrected for multiple comparisons.

Supplementary Figure 24

Two-way ANOVA: VGLUT3 signal in the MEC

Source	Sum Square (10^4)	*df*	MS(10^4)	*F*	*p*
Age	11.34	1	11.34	35.83	= 1e-8
Genotype	19.34	1	19.34	61.09	= 3.4e-13
Interaction	2.36	1	2.36	7.46	= 0.0069
Error	61.42	194	0.32		
Total	92.71	197			

Two-way ANOVA: VGLUT1 signal in CA1

Source	Sum Square (10^4)	*df*	MS(10^4)	*F*	*p*
Age	15.28	1	15.28	9.94	= 0.0018
Genotype	631.66	1	631.66	410.95	= 2.1e-58
Interaction	38.18	1	38.18	24.84	= 1e-6
Error	467.27	304	1.54		
Total	1150.26	307			

Supplementary Figure 24. Two-way unbalanced ANOVAs comparing the effects of age, genotype, and interaction on VGLUT3 and VGLUT1 signal levels in the MEC and CA1 respectively.

df= degrees of freedom, MS = mean square.